Nonlinear Systems for Image Processing

Saverio Morfu*, **Patrick Marquié***, **Brice Nofiélé***, and **Dominique Ginhac***

Contents		

I. INTRODUCTION

For almost 100 years, nonlinear science has attracted the attention of researchers to circumvent the limitation of linear theories in the explanation of natural phenomenons. Indeed, nonlinear differential equations can model the behavior of ocean surfaces (Scott, 1999), the recurrence of ice ages (Benzi *et al.*, 1982), the transport mechanisms in living cells

AQ1

* Laboratoire LE2I UMR 5158, Aile des sciences de l'ingénieur, BP 47870 21078 Dijon, Cedex, France

79

(Murray, 1989), the information transmission in neural networks (Izhikevich, 2007; Nagumo *et al.*, 1962; Scott, 1999), the blood pressure propagation in arteries (Paquerot and Remoissenet, 1994), or the excitability of cardiac tissues (Beeler and Reuter, 1977; Keener, 1987). Therefore, nonlinear science appears as the most important frontier for a better understanding of nature (Remoissenet, 1999).

In the recent field of engineering science (Agrawal1, 2002; Zakharov and Wabnitz, 1998), considering nonlinearity has allowed spectacular progress in terms of transmission capacities in optical fibers via the concept of soliton (Remoissenet, 1999). More recently, nonlinear differential equations in many areas of physics, biology, chemistry, and ecology have inspired unconventional methods of processing that transcend the limitations of classical linear methods (Teuscher and Adamatzky, 2005). This growing interest for processing applications based on the properties of nonlinear systems can be explained by the observation that fundamental progress in several fields of computer science sometimes seems to stagnate. Novel ideas derived from interdisciplinary fields often open new directions of research with unsuspected applications (Teuscher and Adamatzky, 2005).

On the other hand, complex processing tasks require intelligent systems capable of adapting and learning by mimicking the behavior of the human brain. Biologically inspired systems, most often described by nonlinear reaction-diffusion equations, have been proposed as convenient solutions to very complicated problems unaccessible to modern von Neumann computers. It was in this context that the concept of the cellular neural network (CNN) was introduced by Chua and Yang as a novel class of information-processing systems with potential applications in areas such as image processing and pattern recognition (Chua and Yang, 1988a, b). In fact, CNN is used in the context of brain science or the context of emergence and complexity (Chua, 1998). Since the pioneer work of Chua, the CNN paradigm has rapidly evolved to cover a wide range of applications drawn from numerous disciplines, including artificial life, biology, chemistry, physics, information science, nonconventional methods of computing (Holden *et al.*, 1991), video coding (Arena *et al.*, 2003; Venetianer *et al.*, 1995), quality control by visual inspection (Occhipinti *et al.*, 2001), cryptography (Caponetto *et al.*, 2003; Yu and Cao, 2006), signal-image processing (Julian and Dogaru, 2002), and so on (see Tetzlaff (2002), for an overview of the applications).

In summary, the past two decades devoted to the study of CNNs have led scientists to solve problems of artificial intelligence by combining the highly parallel multiprocessor architecture of CNNs with the properties inherited from the nonlinear bio-inspired systems. Among the tasks of high computational complexity routinely performed with nonlinear systems are the optimal path in a two-dimensional (2D) vector field (Agladze *et al.*, 1997), image skeletonization (Chua, 1998), finding

the shortest path in a labyrinth (Chua, 1998; Rambidi and Yakovenchuk, 2001), or controlling mobile robots (Adamatzky *et al.*, 2004). However, the efficiency of these nonlinear systems for signal-image processing or pattern recognition does not come only from their biological background. Indeed, the nonlinearity offers an additional dimension lying in the signal amplitude, which gives rise to novel properties not shared by linear systems. Noise removal with a nonlinear dissipative lattice (Comte *et al.*, 1998; Marquié *et al.*, 1998), contrast enhancement based on nonlinear oscillators properties (Morfu and Comte, 2004), edge detection exploiting vibration noise (Hongler *et al.*, 2003), optimization by noise of nonoptimum problems or signal detection aided by noise via the stochastic resonance phenomenon (Chapeau-Blondeau, 2000; Comte and Morfu, 2003; Gammaitoni *et al.*, 1998) constitute a *nonrestrictive list* of examples in which the properties of nonlinear systems have allowed overcoming the limitations of classical linear approaches.

Owing to the rich variety of potential applications inspired by nonlinear systems, the efforts of researchers have focused on the experimental realization of such efficient information-processing devices. Two different strategies were introduced (Chua and Yang, 1988a; Kuhnert, 1986), and today, the fascinating challenge of artificial intelligence implementation with CNN is still being investigated.

The first technique dates from the late 1980s with the works of Kuhnert, who proposed taking advantage of the properties of Belousov–Zhabotinsky-type media for image-processing purposes (Kuhnert, 1986; Kuhnert *et al.*, 1989). The primary concept is that each micro-volume of the active photosensitive chemical medium acts as a one-bit processor corresponding to the reduced/oxidized state of the catalyst (Agladze *et al.*, 1997). This feature of chemical photosensitive nonlinear media has allowed implementation of numerous tools for image processing. Edge enhancement, classical operations of mathematical morphology, the restoration of individual components of an image with overlapped components (Rambidi *et al.*, 2002), the image skeletonization (Adamatzky *et al.*, 2002), the detection of urban roads, or the analysis of medical images (Teuscher and Adamatzky, 2005) represent a brief overview of processing tasks computed by chemical nonlinear media. However, even considering the large number of chemical "processors," the very low velocity of trigger waves in chemical media is sometimes incompatible with real-time processing constraints imposed by practical applications (Agladze *et al.*, 1997). Nevertheless, the limitations of these unconventional methods of computing in no way dismiss the efficiency and high prospects of the processing developed with active chemical media (Adamatzky and de Lacy Costello, 2003).

By contrast, analog circuits do not share the weakness of the previous strategy of integration. Therefore, because of their real-time processing

capability, electronic hardware devices constitute the most common way to implement CNNs (Chua and Yang, 1988a). The first step to electronically develop a CNN for image-processing purposes consists of designing an elementary cell. More precisely, this basic unit of CNNs usually contains linear capacitors, linear resistors, and linear and nonlinear controlled sources (Chua and Yang, 1988b; Comte and Marquié, 2003). Next, to complete the description of the network, a coupling law between cells is introduced. Owing to the propagation mechanism inherited from the continuous-time dynamics of the network, the cells do not only interact with their nearest neighbors but also with cells that are not directly connected. Among the applications that can be electronically realized are character recognition (Chua and Yang, 1988), edge filtering (Chen *et al.*, 2006; Comte *et al.*, 2001), noise filtering (Comte *et al.*, 1998; Julián and Dogaru, 2002; Marquié *et al.*, 1998), contrast enhancement, and gray-level extraction with a nonlinear oscillators network (Morfu, 2005; Morfu *et al.*, 2007).

The principle of CNN integration with discrete electronic components is closely related to the development of nonlinear electrical transmission lines (NLTLs) (Remoissenet, 1999). Indeed, under certain conditions (Chua, 1998), the parallel processing of information can be ruled by nonlinear differential equations that also describe the evolution of the voltage at the nodes of an electrical lattice. It is then clear that considering a one-dimensional (1D) lattice allows signal filtering, while extending the concept to a 2D network can provide image processing applications.

The development of NLTLs was motivated mainly by the fact that these systems are quite simple and relatively that inexpensive experimental devices allow quantitative study of the properties of nonlinear waves (Scott, 1970). In particular, since the pioneering works by Hirota and Suzuki (1970) and Nagashima and Amagishi (1978) on electrical lines simulating the Toda lattice (Toda, 1967), these NLTLs, which can be considered as analog simulators, provide a useful way to determine the behavior of excitations inside the nonlinear medium (Jäger, 1985; Kuusela, 1995; Marquié *et al.*, 1995; Yamgoué *et al.*, 2007).

This chapter is devoted primarily to the presentation of a few particular nonlinear processing tools and discusses their electronic implementation with discrete components.

After a brief mechanical description of nonlinear systems, we present a review of the properties of both purely inertial systems and overdamped systems. The following sections show how taking advantage of these properties allows the development of unconventional processing methods. Especially considering the features of purely inertial systems, we show how it is possible to perform various image-processing tasks, such as contrast enhancement of a weakly contrasted picture, extraction of gray levels, or encryption of an image. The electronic sketch of the elementary cell of this

inertial CNN is proposed, and the nonlinear properties that allows the previous image processing tasks are experimentally investigated.

The third part of this chapter is devoted exclusively to the filtering applications inspired by reaction-diffusion media—for example, noise filtering, edge detection, or extraction of interest regions in a weakly noisy contrasted picture. In each case, the elementary cell of the electronic CNN is developed and we experimentally investigate its behavior in the specific context of signal-image processing. We conclude by discussing the possible microelectronic implementations of the previous nonlinear systems. In addition, the last section contains some perspectives for future developments inspired by recent properties of nonlinear systems. In particular, we present a paradoxical nonlinear effect known as *stochastic resonance* (Benzi *et al.*, 1982; Chapeau-Blondeau, 1999; Gammaitoni *et al.*, 1998), which is purported to have potential applications in visual perception (Simonotto *et al.*, 1997).

AQ:2

We trust that the multiple topics in this contribution will assist readers in better understanding the potential applications based on the properties of nonlinear systems. Moreover, the various electronic realizations presented constitute a serious background for future experiments and studies devoted to nonlinear phenomena. As it is written for an interdisciplinary readership of physicist and engineers, it is our hope that this chapter will encourage readers to perform their own experiments.

II. MECHANICAL ANALOGY

In order to understand the image-processing tools inspired by the properties of nonlinear systems, we present a mechanical analogy of these nonlinear systems. From a mechanical point of view, we consider a chain of particles of mass M submitted to a nonlinear force f deriving from a potential Φ and coupled with springs of strength D. If W_n represents the displacement of the particle n, the fundamental principle of the mechanics is written as

$$M\frac{d^2W_n}{dt^2} + \lambda\frac{dW_n}{dt} = -\frac{d\Phi}{dW_n} + R_n, \tag{1}$$

where $M\dfrac{d^2W}{dt^2}$ represents the inertia term and $\lambda\dfrac{dW}{dt}$ corresponds to a friction force. Furthermore, the resulting elastic force R_n applied to the nth particle by its neighbors can be defined by:

$$R_n = D\sum_{j\in Nr}\left(W_j - W_n\right), \tag{2}$$

where Nr is the neighborhood, namely, $Nr = \{n-1, n+1\}$ in the case of a 1D chain.

We propose to investigate separately the purely inertial case, that is $M\dfrac{d^2W}{dt^2} >> \lambda\dfrac{dW}{dt}$, and the overdamped one deduced when $M\dfrac{d^2W}{dt^2} << \lambda\dfrac{dW}{dt}$.

A. Overdamped Case

In this section, an overdamped system is presented by neglecting the inertia term of Eq. (1) compared to the friction force. We specifically consider $\lambda = 1$ and the case of a cubic nonlinear force

$$f(W) = -W(W-\alpha)(W-1), \tag{3}$$

deriving from the double-well potential $\Phi(W) = -\int_0^W f(u)du$ as represented in Figure 1 for different values of α. The roots of the nonlinear force 0 and 1 correspond to the positions of the local minima of the potential, namely, the well bottoms, whereas the root α represents the position of the potential maximum. The nonlinearity threshold α defines the potential barrier Δ between the potential minimum with the highest energy and the potential maximum. To explain the propagation mechanism in this chain, it is convenient to define the *excited state* by the position of the potential minimum with the highest energy, and the *rest state* by the position corresponding to the minimum of the potential energy. As shown in Figure 1a,
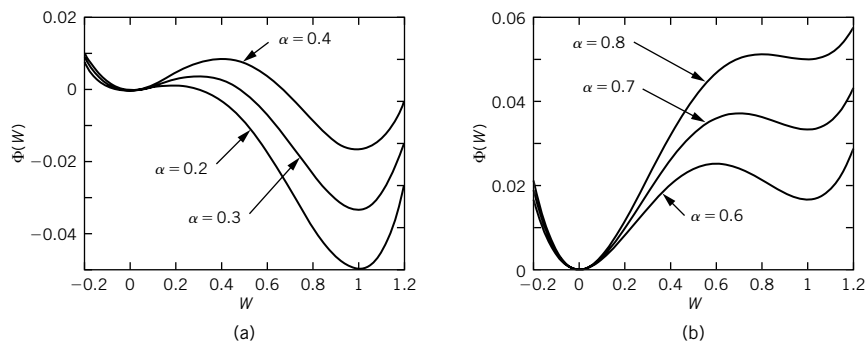

FIGURE 1   Double-well potential deduced from the nonlinear force (3). (a) For $\alpha < 1/2$ the well bottom with highest energy is located at $W = 0$, the potential barrier is given by $\Delta = \int_0^\alpha f(u)du = \phi(\alpha) - \phi(0)$. (b) For $\alpha > 1/2$ the symmetry of the potential is reversed: $W = 1$ becomes the position of the well bottom of highest energy, and the potential barrier is $\Delta = \int_1^\alpha f(u)du = \phi(\alpha) - \phi(1)$.

the excited state is 0 and the rest state is 1 when the nonlinearity threshold $\alpha < 1/2$. In the case $\alpha > 1/2$, since the potential symmetry is reversed, the excited state becomes 1 and the rest state is 0 (Figure 1b). The equation that rules this overdamped nonlinear systems can be deduced from Eq. (1). Indeed, when the second derivative versus time is neglected compared to the first derivative and when $\lambda = 1$, Eq. (1) reduces to the discrete version of Fisher's equation, introduced in the 1930s as a model for genetic diffusion (Fisher, 1937):

$$\frac{dW_n}{dt} = D(W_{n+1} + W_{n-1} - 2W_n) + f(W_n). \tag{4}$$

1. Uncoupled Case

We first investigate the uncoupled case, that is, $D = 0$ in Eq. (4), to determine the bistability of the system. The behavior of a single particle of displacement W and initial position W^0 obeys

$$\frac{dW}{dt} = -W(W - \alpha)(W - 1). \tag{5}$$

The zeros of the nonlinear force f, $W = 1$ and $W = 0$ correspond to stable steady states, whereas the state $W = \alpha$ is unstable. The stability analysis can be realized by solving Eq. (5) substituting the nonlinear force $f = -W(W - \alpha)(W - 1)$ for its linearized expression near the considered **AQ:3** steady states $W^* \in \{0, 1, \alpha\}$. If $f_W(W^*)$ denotes the derivative versus W of the nonlinear force for $W = W^*$, we are led to solve:

$$\frac{dW}{dt} = f_W(W^*)(W - W^*) + f(W^*). \tag{6}$$

The solution of Eq. (6) can then be easily expressed as

$$W(t) = W^* + Ce^{f_W(W^*)t} - \frac{f(W^*)}{f_W(W^*)} \tag{7}$$

where C is a constant depending on the initial condition—the initial position of the particle. The solution in Eq. (7), obtained with a linear approximation of the nonlinear force f, shows that the stability is set by the sign of the argument of the exponential function.

Indeed, for $W^* = 0$ and $W^* = 1$, the sign of $f_W(W^*)$ is negative, involving that $W(t \mapsto \infty)$ tends to a constant. Therefore, the two points $W^* = 0$ and $W^* = 1$ are stable steady states. Conversely, for $W^* = \alpha$, $f_W(W^*)$ is

positive, inducing a divergence for $W(t \mapsto \infty)$. $W^* = \alpha$ is an unstable steady state.

We now focus our attention on the particular case $\alpha = 1/2$ since it will allow interesting applications in signal and image processing.

This case is intensively developed in Appendix A, where it is shown that the displacement of a particle with initial position W^0 can be expressed by

$$W(t) = \frac{1}{2}\left(1 + \frac{W^0 - \frac{1}{2}}{\sqrt{(W^0 - \frac{1}{2})^2 - W^0(W^0 - 1)e^{-\frac{1}{2}t}}}\right). \tag{8}$$

This theoretical expression is compared in Figure 2 to the numerical results obtained solving Eq. (5) using a fourth-order Runge–Kutta algorithm with integrating time step $dt = 10^{-3}$. As shown in Figure 2, when the initial condition W^0 is below the unstable state $\alpha = 1/2$, the particle evolves toward the steady state 0. Otherwise, if the initial condition W^0 exceeds the unstable state $\alpha = 1/2$, the particle evolves toward the other steady state 1. Therefore, the unstable states $\alpha = 1/2$ acts as a threshold and the system exhibits a bistable behavior.
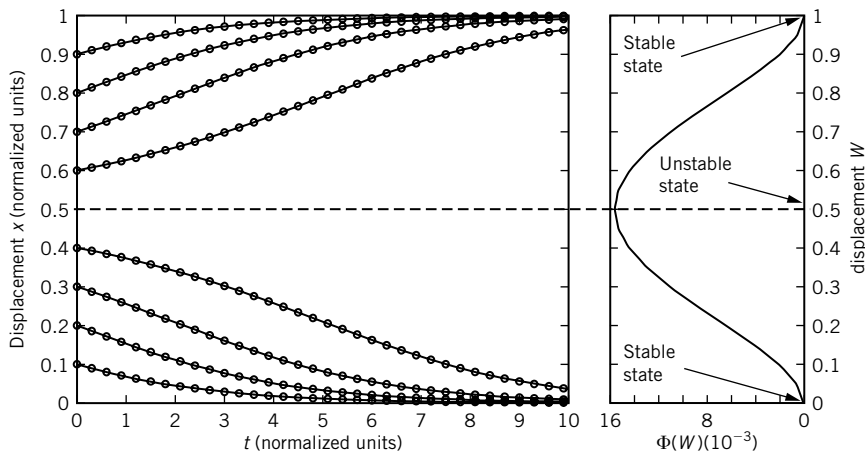

FIGURE 2 Bistable behavior of the overdamped system in the case $\alpha = 1/2$. Left: Evolution of a particle for different initial conditions in the range [0; 1]. The solid line is plotted with the analytical expression in Eq. (8), whereas the (*o*) signs correspond to the numerical solution of Eq. (5) for different initial conditions $W^0 \in [0; 1]$. The potential ϕ obtained by integrating the nonlinear force (3) is represented at the right as a reference.

2. Coupled Case

We now consider the coupled case ($D \neq 0$). In such systems ruled by Eq. (4), the balance between the dissipation and the nonlinearity gives rise to the propagation of a kink (a localized wave) called a *diffusive soliton* that propagates with constant velocity and profile (Remoissenet, 1999). To understand the propagation mechanism, we first consider the weak coupling limit and the case $\alpha < 1/2$. The case of strong coupling, which corresponds to a continuous medium, is discussed later since it allows theoretical characterization of the waves propagating in the medium.

a. Weak Coupling Limit. As shown in Figure 3a, initially all particles of the chain are located at the position 0—the excited state. To initiate a kink, an external forcing allows the first particle to cross the potential barrier in $W = \alpha$ and to fall in the right well, at the rest state defined by the position $W = 1$. Thanks to the spring coupling the first particle to the second one, but despite the second spring, the second particle attempts to cross the potential barrier with height $\Delta(\alpha) = -\dfrac{\alpha^4}{12} + \dfrac{\alpha^3}{6}$ (Morfu, 2003) (see Figure 3b).
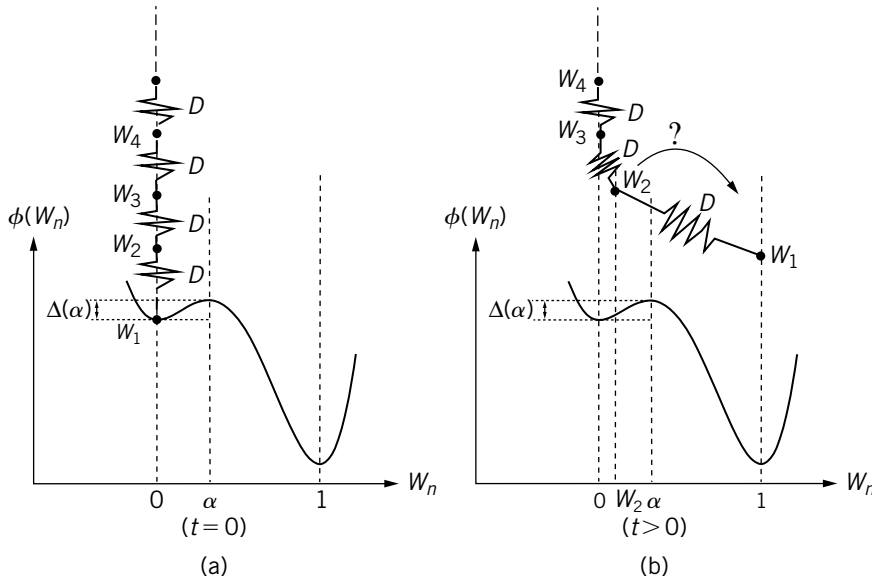

FIGURE 3 Propagation mechanism. (a) Initially all particles of the chain are in the excited state 0, that is, at the bottom of the well with highest energy. (b) State of the chain for $t > 0$. The first particle has crossed the potential barrier Δ and attempts to pull the second particle down in its fall.

According to the value of the resulting force applied to the second particle by the two springs compared to the nonlinear force f between $[0, \alpha[$, two behaviors may occur:

1. If the resulting elastic force is sufficiently important to allow the second particle to cross the potential barrier $\Delta(\alpha)$, then this particle falls in the right well and pulls the next particle down in its fall. Since each particle of the chain successively undergoes a transition from the excited state 0 to the rest state 1, a kink propagates in the medium. Moreover, its velocity increases versus the coupling and as the barrier decreases (namely, as α decreases).
2. Otherwise, if the resulting force does not exceed a critical value (i.e., if $D < D^*(\alpha)$), the second particle cannot cross the potential barrier and thus stays pinned at a position w in $[0; \alpha[$: it is the well-known propagation failure effect (Comte *et al.*, 2001; Erneux and Nicolis, 1993; Keener, 1987; Kladko *et al.*, 2000).

The mechanical model associated with Eq. (4) shows that in the weak coupling limit the characteristics of the nonlinear system are ruled by the coupling D and the nonlinear threshold α. Moreover, the propagation of a kink is due to the transition from the excited state to the rest state and is only possible when the coupling D exceeds a critical value $D^*(\alpha)$.

b. Limit of Continuous Media.   The velocity of the kink and its profile can be theoretically obtained in the limit of continuous media—when the coupling D is large enough compared to the nonlinear strength.

Then, in the continuous limit, the discrete Laplacian of Eq. (4) can be replaced by a second derivative versus the space variable z:

$$\frac{\partial W}{\partial t} = D\frac{\partial^2 W}{\partial z^2} + f(W). \tag{9}$$

This equation, introduced by Nagumo in the 1940s as an elementary representation of the conduction along an active nerve fiber, has an important meaning in understanding transport mechanism in biological systems (Murray, 1989; Nagumo *et al.*, 1962).

Unlike the discrete Equation (4), the continuous Equation (9) admits propagative kink solution only if $\int_0^1 f(u)du \neq 0$, which reduces to $\alpha \neq 1/2$ in the case of the cubic force (3) (Scott, 1999).

Introducing the propagative variable $\xi = z - ct$, these kinks and anti-kinks have the form (Fife, 1979; Henry, 1981)

$$W(\xi) = \frac{1}{2}\left[1 \pm \tanh\left(\frac{1}{2\sqrt{2D}}(\xi - \xi_0)\right)\right], \tag{10}$$

where ξ_0 is the initial position of the kink for $t = 0$ and where the kink velocity is defined by $c = \pm\sqrt{D/2}(1 - 2\alpha)$.

When $\alpha < 1/2$, the excited state is 0, and the rest state is 1. Therefore, the rest state 1 spreads in the chain, which set the sign of the velocity according to the profile of the kink initiated in the nonlinear system:

1. If the profile is given by $W(\xi) = \frac{1}{2}\left[1 - \tanh\left(\frac{1}{2\sqrt{2D}}(\xi - \xi_0)\right)\right]$, a kink propagates from left to right with a positive velocity $c = \sqrt{D/2}(1 - 2\alpha)$ (Figure 4a, left).

2. Otherwise, if the profile is set by $W(\xi) = \frac{1}{2}\left[1 + \tanh\left(\frac{1}{2\sqrt{2D}}(\xi - \xi_0)\right)\right]$, a kink propagates from right to left with a negative velocity $c = -\sqrt{D/2}(1 - 2\alpha)$ (Figure 4a, right).

When $\alpha > 1/2$, since the symmetry of the potential is reversed, the excited state becomes 1 and the rest state is 0. The propagation is then due to a transition between 1 and 0, which provides the following behavior:

1. If $W(\xi) = \frac{1}{2}\left[1 - \tanh\left(\frac{1}{2\sqrt{2D}}(\xi - \xi_0)\right)\right]$, a kink propagates from right to left with a negative velocity $c = \sqrt{D/2}(1 - 2\alpha)$ (Figure 4b, left).
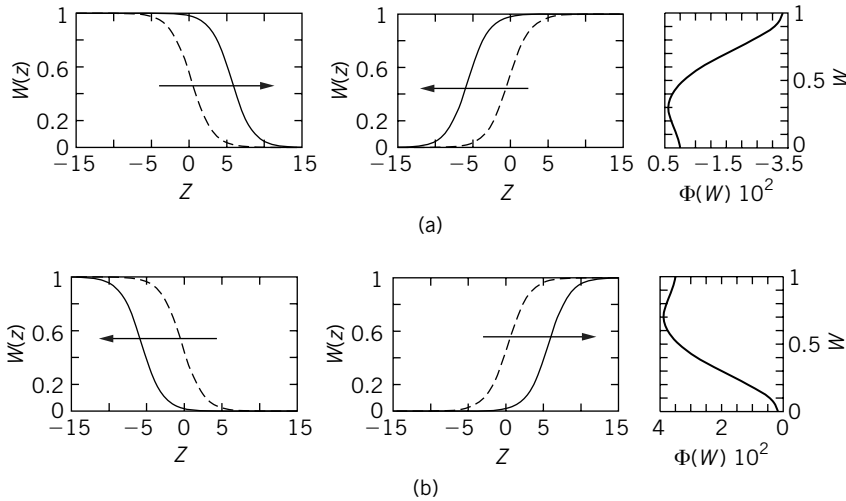

FIGURE 4 Propagative solution of the continuous Nagumo Equation (9) with $D = 1$. Spatial representation of the kink for $t = 0$ in dotted line and for $t = 20$ in solid line. The arrow indicates the propagation direction, the corresponding potential is represented at the right end to provide a reference. (a) $\alpha = 0.3$, (b) $\alpha = 0.7$.

2. Else if $W(\xi) = \frac{1}{2}\left[1 + \tanh\left(\frac{1}{2\sqrt{2D}}(\xi - \xi_0)\right)\right]$, a kink propagates from left to right with a positive velocity $c = -\sqrt{D/2}(1 - 2\alpha)$ (Figure 4b, right).

B. Inertial Systems

In this section, we neglect the dissipative term of Eq. (1) compared to the inertia term and we restrict our study to the uncoupled case. Moreover, in image-processing context, it is convenient to introduce a nonlinear force f under the form

$$f(W) = -\omega_0^2(W - m)(W - m - \alpha)(W - m + \alpha), \tag{11}$$

where, m and $\alpha < m$ are two parameters that allow adjusting the width and height $\Delta = \omega_0^2\alpha^4/4$ of the potential Φ (Figure 5):

$$\Phi(W) = -\int_0^W f(u)du. \tag{12}$$

The nonlinear differential equation that rules the uncoupled chain can be deduced by inserting the nonlinear force (11) into Eq. (1) with $D = 0$.
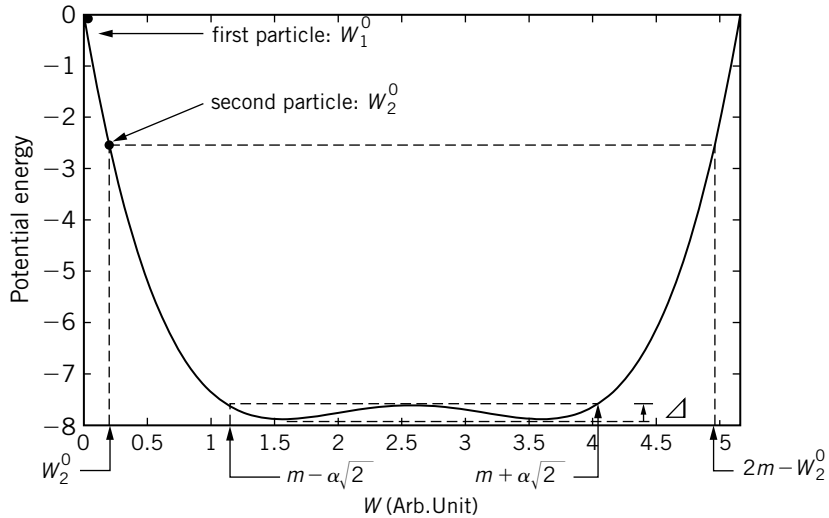

FIGURE 5 Double-well potential deduced from the nonlinear force (11) represented for $m = 2.58$, $\alpha = 1.02$, and $\omega_0 = 1$. A particle with an initial condition $W_i^0 < m - \alpha\sqrt{2}$ evolves with an initial potential energy above the barrier Δ.

Neglecting the dissipative term, the particles of unitary mass are then ruled by the following nonlinear oscillator equations:

$$\frac{d^2 W_i}{dt^2} = f(W_i). \tag{13}$$

1. Theoretical Analysis

We propose here to determine analytically the dynamics of the nonlinear oscillators obeying Eq. (13) (Morfu and Comte, 2004; Morfu *et al.*, 2006). Setting $x_i = W_i - m$, Eq. (13) can be rewritten as

$$\frac{d^2 x_i}{dt^2} = -\omega_0^2 x_i (x_i - \alpha)(x_i + \alpha). \tag{14}$$

Noting x_i^0 the initial position of the particle i and considering that all the particles initially have a null velocity, the solutions of Eq. (14) can be expressed with the Jacobian elliptic functions as

$$x_i(t) = x_i^0 cn(\omega_i t, k_i), \tag{15}$$

where ω_i and $0 \le k_i \le 1$ represent, respectively, the pulsation and the modulus of the *cn* function (see recall on the properties of Jacobian elliptic function in Appendix B).

Deriving Eq. (15) twice and using the properties in Eq. (B3), yields

$$\frac{dx_i}{dt} = -x_i^0 \omega_i sn(\omega_i t, k_i) dn(\omega_i t, k_i),$$

$$\frac{d^2 x_i}{dt^2} = -x_i^0 \omega_i^2 cn(\omega_i t, k_i) \left[dn^2(\omega_i t, k_i) - k_i sn^2(\omega_i t, k_i) \right]. \tag{16}$$

Using the identities in Eq. (B4) and (B5), Eq. (16) can be rewritten as

$$\frac{d^2 x_i}{dt^2} = -\frac{2k_i \omega_i^2}{x_i^{0^2}} x \left[x^2 - \frac{2k_i - 1}{2k_i} x_i^{0^2} \right]. \tag{17}$$

Identifying this last expression with Eq. (14), we derive the pulsation of the Jacobian elliptic function

$$\omega_i = \omega_0 \sqrt{x_i^{0^2} - \alpha^2}, \tag{18}$$

and its modulus

$$k_i = \frac{1}{2} \frac{x_i^{0^2}}{x_i^{0^2} - \alpha^2}. \tag{19}$$

Finally, introducing the initial condition $W_i^0 = x_i^0 + m$, the solution of Eq. (13) can be straightforwardly deduced from Eqs. (15), (18), and (19):

$$W_i(t) = m + (W_i^0 - m)cn(\omega_i t, k_i), \tag{20}$$

with

$$\omega_i(W_i^0) = \omega_0 \sqrt{(W_i^0 - m)^2 - \alpha^2} \quad \text{and} \quad k_i(W_i^0) = \frac{1}{2} \frac{(W_i^0 - m)^2}{(W_i^0 - m)^2 - \alpha^2}. \tag{21}$$

Both the modulus and the pulsation are driven by the initial condition W_i^0. Moreover, the constraints to ensure the existence of the pulsation ω_i and of the modulus, respectively, are written as $(W_i^0 - m)^2 - \alpha^2 \geq 0$ and $0 \leq k_i \leq 1$. These two conditions restrict the range of the allowed initial conditions W_i^0 to $]-\infty; \ m - \alpha\sqrt{2}] \bigcup [m + \alpha\sqrt{2}; \ +\infty[$, as shown in Figure 6, where the pulsation and the modulus are represented versus the initial condition W_i^0. Note that this allowed range of initial conditions corresponds also to a particle with an initial potential energy exceeding the barrier Δ between the potential extrema (see Figure 5).

2. Nonlinear Oscillator Properties

To illustrate the properties of nonlinear oscillators, we consider a chain of length $N = 2$ particles with a weak difference of initial conditions and with a null initial velocity. The dynamics of these two oscillators are ruled by Eq. (20), where the pulsation and modulus of both oscillators are driven by their respective initial condition. Moreover, we have restricted our study to the case of the following nonlinearity parameters $m = 2.58$, $\alpha = 1.02$, $\omega_0 = 10^4$. We have applied the initial condition $W_1^0 = 0$ to the first oscillator, while the initial condition of the second oscillator is set to $W_2^0 = 0.2$, which corresponds to the situation of Figure 5.

Figure 7a shows that the oscillations of both particles take place in the range $[W_i^0; \ 2m - W_i^0]$ as predicted by Eq. (20) [that is, [0; 5.16] for the first oscillator and [0; 4.96] for the second one]. Moreover, owing to their difference of initial amplitude and to the nonlinear behavior of the system, the two oscillators quickly attain a phase opposition for the first time at $t = t_{opt} = 1.64 \times 10^{-3}$. This phase opposition corresponds to the
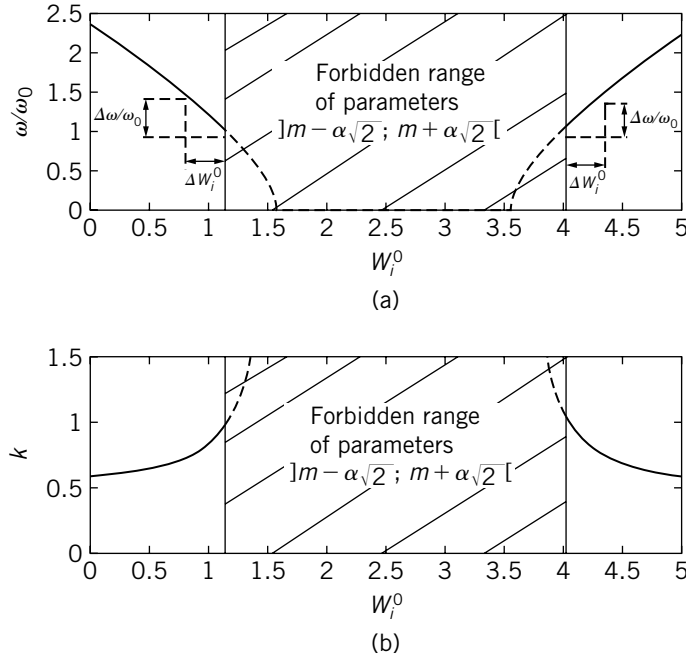
FIGURE 6 (a): Normalized pulsation ω/ω_0 versus the initial condition W_i^0.
(b) Modulus parameter k versus W_i^0. The parameters of the nonlinearity $m = 2.58$,
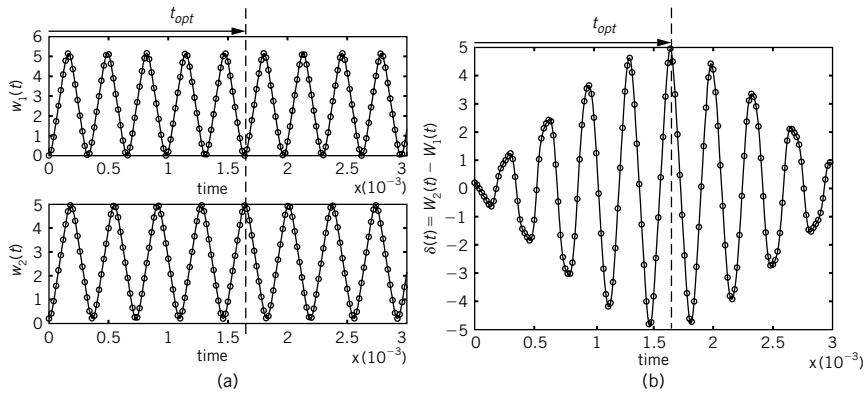$\alpha = 1.02$ impose the allowed amplitude range $]-\infty; 1.137] \bigcup [4.023; +\infty[$.

FIGURE 7 (a) Temporal evolution of the two oscillators. Top panel: evolution of
the first oscillator with initial condition $W_1^0 = 0$. Bottom panel: evolution of the
second oscillator with initial condition $W_2^0 = 0.2$. (b) Temporal evolution of the
displacement difference δ between the two oscillators. Parameters: $m = 2.58$, $\alpha = 1.02$,
and $\omega_0 = 1$.

situation where the first oscillator has reached its minimum $W_1(t_{opt}) = 0$, whereas the second oscillator has attained its maximum $W_2(t_{opt}) = 4.96$. As shown in Figure 7b, the displacement difference $\delta(t) = W_2(t) - W_1(t)$ is then maximum for $t = t_{opt}$ and becomes $\delta(t_{opt}) = 4.96$. For this optimal time, a "contrast enhancement" of the weak difference of initial conditions is realized, since initially the displacement difference was $\delta(t = 0) = 0.2$. Note that in Figure 7b, the displacement difference between the two oscillators also presents a periodic behavior with local minima and local maxima. In particular, the difference $\delta(t)$ is null for $t = 3.96 \times 10^{-5}$, $t = 1.81 \times 10^{-4}$, $t = 3.5 \times 10^{-4}$, $t = 5.21 \times 10^{-4}$; minimum for $t = 1.4 \times 10^{-4}$, $t = 4.64 \times 10^{-4}$, $t = 1.47 \times 10^{-3}$ and maximum for $t = 3 \times 10^{-4}$, $t = 6.29 \times 10^{-4}$, $t = 1.64 \times 10^{-3}$. These characteristic times will be of crucial interest in image-processing context to define the filtered tasks performed by the nonlinear oscillators network.

Figure 6a reveals that the maximum variation of the pulsation compared to the amplitude W_i^0, that is, $\Delta\omega/\omega_0$, is reached for $W_i^0 = m - \alpha\sqrt{2}$, that is, for a particle with an initial potential energy near the barrier Δ. Therefore, to quickly realize a great amplitude contrast between the two oscillators, it could be interesting to launch them with an initial amplitude near $m - \alpha\sqrt{2}$, or to increase the potential barrier height Δ. We chose to investigate this latter solution by tuning the parameter of the nonlinearity α, when the initial amplitude of both oscillators remains $W_1^0 = 0$ and $W_2^0 = 0.2$. The results are reported in Figure 8, where we present the evolution of the difference $\delta(t)$ for different values of α.

As expected, when the nonlinearity parameter α increases, the optimal time is significantly reduced. However, when α is adjusted near the critical value $(m - W_2^0)/\sqrt{2}$ as in Figure 8d, the optimum reached by the difference $\delta(t)$ is reduced to 4.517 for $\alpha = 1.63$ instead of 4.96 for $\alpha = 1.02$. Even if it is not the best contrast enhancement that can be performed by the system, the weak difference of initial conditions between the two oscillators is nevertheless strongly enhanced for $\alpha = 1.63$.

To highlight the efficiency of nonlinear systems, let us consider the case of a linear force $f(W) = -\omega_0 W$ in Eq. (13).

In the linear case, the displacement difference $\delta(t)$ between two harmonic oscillators can be straightforwardly expressed as

$$\delta(t) = \epsilon \cos(\omega_0 t), \tag{22}$$

where ϵ represents the slight difference of initial conditions between the oscillators. This last expression shows that it is impossible to increase the weak difference of initial conditions since the difference $\delta(t)$ always remains in the range $[-\epsilon; \epsilon]$. Therefore, nonlinearity is a convenient solution to overcome the limitation of a linear system and to enhance a weak amplitude contrast.
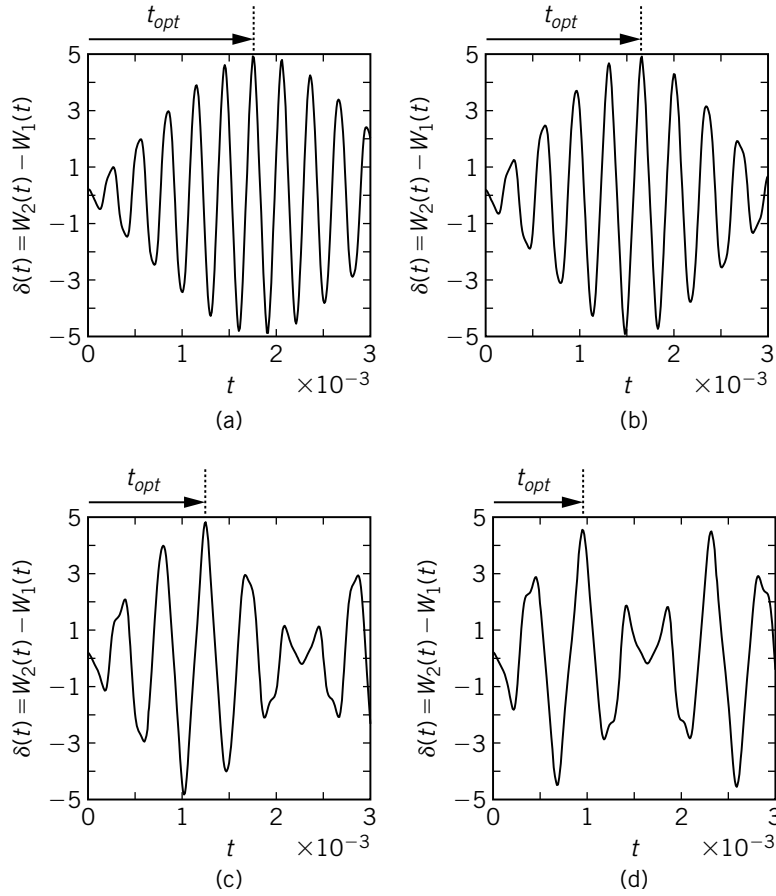
FIGURE 8   Influence of the nonlinearity parameter α on the displacement difference δ between the two oscillators of respective initial conditions 0 and 0.2. Parameters $m = 2.58$ and $\omega_0 = 1$. (a): ($t_{opt} = 1.75 \times 10^{-3}; \alpha = 0.4$). (b): ($t_{opt} = 1.66 \times 10^{-3}$; $\alpha = 1.05$). (c): ($t_{opt} = 1.25 \times 10^{-3}; \alpha = 1.5$). (d): ($t_{opt} = 0.95 \times 10^{-3}; \alpha = 1.63$).

III. INERTIAL SYSTEMS

This section presents different image-processing tasks inspired by the properties of the nonlinear oscillators presented in Section II.B. Their electronic implementation is also discussed.

A. Image Processing

By analogy with a particle experiencing a double-well potential, the pixel number (i, j) is analog to a particle (oscillator) whose initial position

corresponds to the initial gray level $W_{i,j}^0$ of this pixel. Therefore, if $N \times M$ denotes the image size, we are led to consider a 2D network, or CNN, consisting of uncoupled nonlinear oscillators. The node i, j of this CNN relates to

$$\frac{d^2 W_{i,j}}{dt^2} = -\omega_0^2 (W_{i,j} - m - \alpha)(W_{i,j} - m + \alpha)(W_{i,j} - m), \qquad (23)$$

with $i = 1, 2 \ldots N$ and $j = 1, 2 .. , M$.

Note that we take into account the range of oscillations $[0; \ 2m - W_{i,j}^0]$ predicted in Section II.B.2 to define the gray scale of the images, namely, 0 for the black level and $2m = 5.16$ for the white level.

The image to be processed is first loaded as the initial condition at the nodes of the CNN. Next, the filtered image for a processing time t can be deduced noting the position reached by all oscillators of the network at this specific time t. More precisely, the state of the network at a processing time t is obtained by solving numerically Eq. (23) with a fourth-order Runge–Kutta algorithm with integrating time step $dt = 10^{-6}$.

1. Contrast Enhancement and Image Inversion

The image to process with the nonlinear oscillator network is the weak contrasted image of Figure 9a. Its histogram is restricted to the range $[0; \ 0.2]$, which means that the maximum gray level of the image (0.2) is the initial condition of at least one oscillator of the network, while the minimum gray level of the image (0) is also the initial condition of at least one oscillator. Therefore, the pixels with initial gray level 0 and 0.2 oscillate with the phase difference $\delta(t)$ predicted by Figure 7b. In particular, as explained in Section II.B.2, their phase difference $\delta(t)$ can be null for the processing times $t = 3.96 \times 10^{-4}, 1.81 \times 10^{-4}, 3.5 \times 10^{-4}$, and 5.21×10^{-4}; minimum for $t = 1.4 \times 10^{-4}, 4.64 \times 10^{-4}$, and 1.47×10^{-3} and maximum for $t = 3 \times 10^{-4}, 6.29 \times 10^{-3}$, and 1.64×10^{-3}. As shown in Figure 9b, 9d, 9f, and 9h, the image goes through local minima of contrast at the processing times corresponding to the zeros of $\delta(t)$. Furthermore, the processing times providing the local minima of $\delta(t)$ realize an image inversion with a growing contrast enhancement (Figure 9c, 9g, and 9j). Indeed, since the minima of $\delta(t)$ are negative, for these processing times the minimum of the initial image becomes the maximum of the filtered image and vice versa. Finally, the local maxima of $\delta(t)$ achieve local maxima of contrast for the corresponding processing times (Figure 9e, 9i, and 9k). Note that the best enhancement of contrast is attained at the processing time t_{opt} for which $\delta(t)$ is maximum. The histogram of each filtered image in Figure 9 also reveals the temporal dynamic of the network. Indeed, the width of the image histogram is periodically increased and decreased, which indicates that the
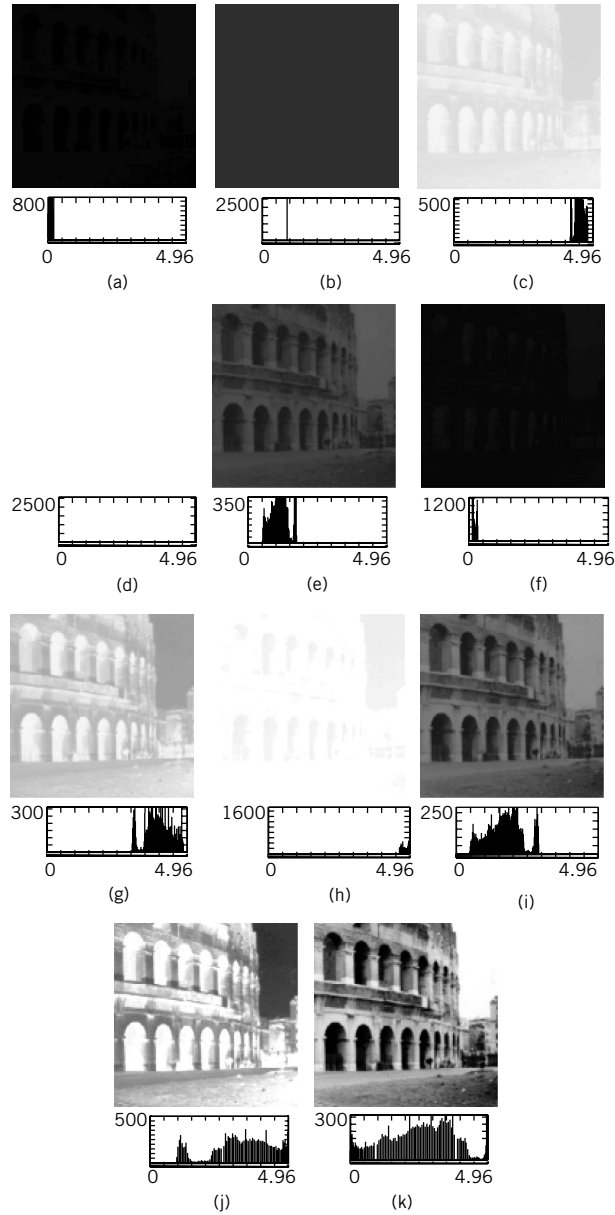
FIGURE 9   Filtered images and their corresponding histogram obtained with the nonlinear oscillators network (23) for different processing times. (a) Initial image ($t = 0$). (b) $t = 3.96 \times 10^{-5}$. (c) $t = 1.4 \times 10^{-4}$. (d) $t = 1.81 \times 10^{-4}$. (e) $t = 3 \times 10^{-4}$. (f) $t = 3.5 \times 10^{-4}$. (g) $t = 4.64 \times 10^{-4}$. (h) $t = 5.21 \times 10^{-4}$. (i) $t = 6.29 \times 10^{-4}$. (j) $t = 1.47 \times 10^{-3}$. (k) $t = t_{opt} = 1.64 \times 10^{-3}$. **Parameters:** $m = 2.58$, $\alpha = 1.02$, $\omega_0 = 1$.

contrast of the corresponding filtered image is periodically enhanced or reduced.

Another interesting feature of the realized contrast is determined by the plot of the network response at the processing time t_{opt} (Morfu, 2005). This curve also represents the gray level of the pixels of the filtered image versus their initial gray level. Therefore, the horizontal axis corresponds to the initial gray scale, namely, [0; 0.2], whereas the vertical axis represents the gray scale of the processed image. Such curves are plotted in Figure 10 for different values of the nonlinearity parameter α, and at the optimal time defined by the maximum of $\delta(t)$. In fact, these times were established in Section II.B.2 in Figure 8.

Moreover, to compare the nonlinear contrast enhancement to a uniform one, we have superimposed (dotted line) the curve resulting from a simple multiplication of the initial gray scale by a scale factor. In Figure 10a, since the response of the system for the lowest value of α is most often above the dotted line, the filtered image at the processing time $t_{opt} = 1.75 \times 10^{-3}$ for $\alpha = 0.4$ will be brighter than the image obtained with a simple rescaling.
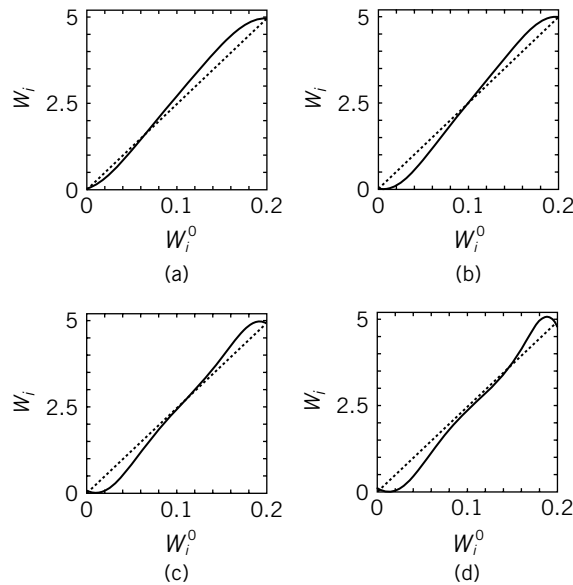

FIGURE 10   Response of the nonlinear system for different nonlinearity parameters α at the corresponding optimal time t_{opt} (solid line) compared to a uniform rescaling (dotted line). The curves are obtained with Eqs. (20) and (21) setting the time to the optimum value defined by the maximum of $\delta(t)$ (see Figure 8). In addition, we let the initial conditions W_i^0 vary in the range [0; 0.2] in Eqs. (20) and (21). (a): ($t_{opt} = 1.75 \times 10^{-3}$; $\alpha = 0.4$). (b): ($t_{opt} = 1.66 \times 10^{-3}$; $\alpha = 1.05$). (c): ($t_{opt} = 1.25 \times 10^{-3}$; $\alpha = 1.5$). (d): ($t_{opt} = 0.95 \times 10^{-3}$; $\alpha = 1.63$), $\omega_0 = 1$.

As shown in Figure 10b, increasing the nonlinearity parameter α to 1.05 involves an optimum time 1.66×10^{-3} and symmetrically enhances the light and dark gray levels. When the nonlinearity parameter is adjusted to provide the greatest potential barrier (Figure 10c and 10d), the contrast of the medium gray level is unchanged compared to a simple rescaling. Moreover, the dark and light grays are strongly enhanced with a greater distortion when the potential barrier is maximum, that is, for the greatest value of α (Figure 10d).

2. Gray-Level Extraction

Considering processing times exceeding the optimal time t_{opt}, we propose to perform a gray-level extraction of the continuous gray scale represented in Figure 11a (Morfu, 2005). For the sake of clarity, it is convenient to redefine the white level by 0.2, whereas the black level remains 0.

For the nine specific times presented in Figure 11, the response of the system displays a minimum that is successively reached for each level of the initial gray scale. Therefore, with time acting as a discriminating parameter, an appropriate threshold filtering allow extraction of all pixels with a gray level in a given range. Indeed, in Figure 11, the simplest case of a constant threshold $V_{th} = 0.25$ provides nine ranges of gray at nine closely different processing times, which constitutes a gray-level extraction.

Moreover, owing to the response of the system, the width of the extracted gray-level ranges is reduced in the light gray. Indeed, the range extracted in the dark gray for the processing time $t = 3.33 \times 10^{-3}$ (Figure 11c) is approximatively twice greater than the range extracted in the light gray for $t = 3.51 \times 10^{-3}$ (Figure 11i). To perform a perfect gray-level extraction, the threshold must match with a slight offset the temporal evolution of the minimum attained by the response of the system. Under these conditions, the width of the extracted gray range is set by the value of this offset.

Note that the response of the system after the optimal processing times also allow consecutive enhancement of the fragment of the image with different levels of brightness, which is also an important feature of image processing. For instance, in Belousov–Zhabotinsky-type media this property of the system enabled Rambidi *et al.* (2002) to restore individual components of the picture when the components overlap. Therefore, we trust that considering the temporal evolution of the image loaded in our network could give rise to other interesting image-processing operations.

3. Image Encryption

Cryptography is another field of application of nonlinear systems. In fact, the chaotic behavior of nonlinear systems can sometimes produce chaotic like waveforms that can be used to encrypt signals for secure communications (Cuomo and Oppenheim, 1993; Dedieu *et al.*, 1993). Even if
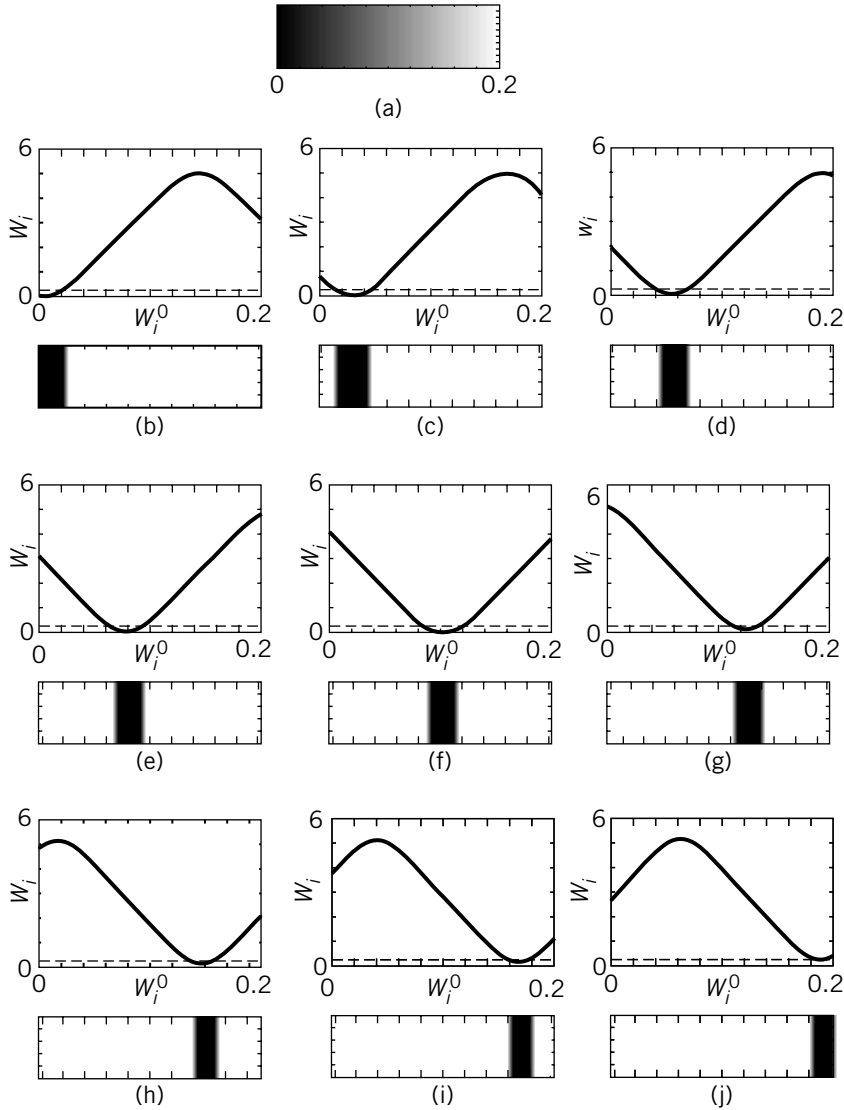
AQ4

FIGURE 11 Gray-level extraction. The response of the system is represented at the top of each figure. At the bottom of each figure, a threshold filtering of the filtered image is realized replacing the pixel gray level with 0.2 (white) if that gray level exceeds the threshold $V_{th} = 0.25$, otherwise with 0 (black). (a) Initial gray scale ($t = 0$). (b) $t = 3.3 \times 10^{-3}$. (c) $t = 3.33 \times 10^{-3}$. (d) $t = 3.36 \times 10^{-3}$. (e) $t = 3.39 \times 10^{-3}$. (f) $t = 3.42 \times 10^{-3}$. (g) $t = 3.45 \times 10^{-3}$. (h) $t = 3.48 \times 10^{-3}$. (i) $t = 3.51 \times 10^{-3}$. (j) $t = 3.54 \times 10^{-3}$. Nonlinearity parameters: $m = 2.58$, $\alpha = 1.02$, and $\omega_0 = 1$

many attempts to break the encryption key of these cryptosystems and to retrieve the information have been reported (Short and Parker, 1998; Udaltsov *et al.*, 2003), cryptography based on the properties of chaotic oscillators still attracts the attention of researchers because of the promising applications of chaos in the data transmission field (Kwok and Tang, 2007).

Contrary to most studies, in which the dynamics of a single element are usually considered, we propose here a strategy of encryption based on the dynamics of a chain of nonlinear oscillators. More precisely, we consider the case of a noisy image loaded as the initial condition in the inertia network introduced in Section II.B. In addition, we add a uniform noise over $[-0.1; 0.1]$ to the weak-contrast picture of the Coliseum represented in Figure 9a. Since the pixels of the noisy image assume a gray level in the range $[-0.1; 0.3]$, an appropriate change of scale is realized to reset the dynamics of the gray levels to $[0; 0.2]$. The resulting image is then loaded as the initial condition in the network. For the sake of clarity, the filtered images are presented at different processing times with the corresponding system response in Figure 12.

Before the optimal time, we observe the behavior described in Section III.A.1: the image goes through local minima and maxima of contrast until the optimum time $t_{opt} = 1.64 \times 10^{-3}$, where the best contrast enhancement is realized (Figure 12a).

Next, for processing times exceeding t_{opt}, the noisy part of the image seems to be amplified while the coherent part of the image begins to be increasingly less perceptible (see Figure 12b and 12c obtained for $t = 3.28 \times 10^{-3}$ and $t = 6.56 \times 10^{-3}$). Finally, for longer processing times, namely, $t = 8.24 \times 10^{-3}$ and $t = 9.84 \times 10^{-3}$, the noise background has completely hidden the Coliseum, which constitutes an image encryption.

Note that this behavior can be explained with the response of the system, as represented below each filtered image in Figure 12. Indeed, until the response of the system versus the initial condition does not display a "periodic-like" behavior, the coherent part of the image remains perceptible (Figure 12a and 12b). By contrast, as soon as a "periodicity" appears in the system response, the coherent image begins to disappear (Figure 12c). Indeed, the response in Figure 12c shows that four pixels of the initial image with four different gray levels take the same final value in the encrypted image (see the arrows). Therefore, the details of the initial image, which corresponds to the quasi-uniform area of the coherent image, are merged and thus disappear in the encrypted image. Despite the previous merging of gray levels, since noise induces sudden changes in the gray levels of the initial image, the noise conserves its random feature in the encrypted image. Moreover, since the system tends to enlarge the range of amplitude, the weak initial amount of noise is strongly amplified whenever the processing time exceeds t_{opt}. The periodicity of
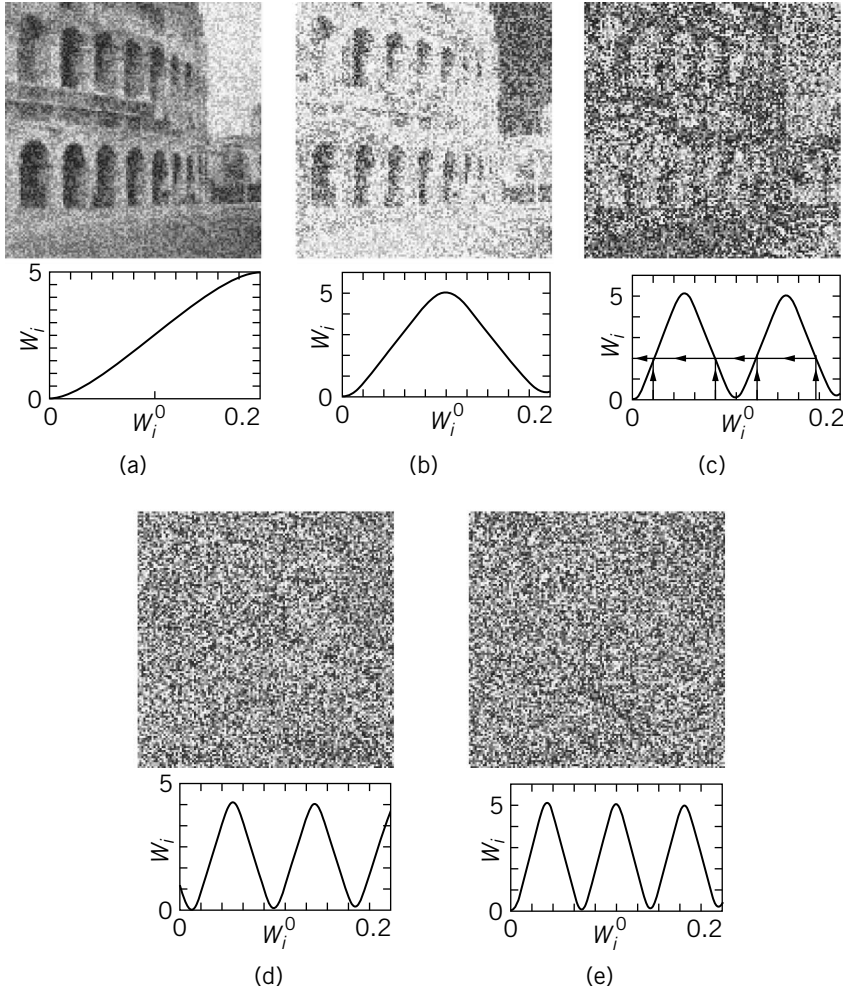
FIGURE 12   Encrypted image and the corresponding response of the nonlinear oscillators network for different times exceeding t_{opt}. (a): Enhancement of contrast of the initial image for $t = t_{opt} = 1.64 \times 10^{-3}$. (b): $t = 3.28 \times 10^{-3}$. (c): $t = 6.56 \times 10^{-3}$. (d): $t = 8.24 \times 10^{-3}$. (e): $t = 9.84 \times 10^{-3}$. **Parameters:** $m = 2.58$, $\alpha = 1.02$, $\omega_0 = 1$.

the system response can then be increased for longer processing times until only the noisy part of the image is perceptible (Figure 12d and 12e). A perfect image encryption is then realized.

To take advantage of this phenomenon for image encryption, the coherent information (the enhanced image in Figure 12a), must be restored using the encrypted image of Figure 12e. Fortunately, owing to the absence of dissipation, the nonlinear systems is conservative and reversible. It is thus

possible to revert to the optimal time—when the information was the most perceptible.

However, the knowledge of the encrypted image is not sufficient to completely restore the coherent information, since at the time of encryption, the velocity of the oscillators was not null. Consequently, it is necessary to know both the position and the velocity of all particles of the network at the time of encryption. The information then can be restored solving numerically Eq. (23) with a negative integrating time step $dt = -10^{-6}$.

Under these conditions, the time of encryption constitutes the encryption key.

B. Electronic Implementation

The elementary cell of the purely inertial system can be developed according to the principle of Figure 13 (Morfu *et al.*, 2007). First, a polynomial source is realized with analog *AD633JNZ* multipliers and classical inverting amplifier with gain $-K$. Taking into account the scale factor $1/10\ V^{-1}$ of the multipliers, the response of the nonlinear circuit to an input voltage

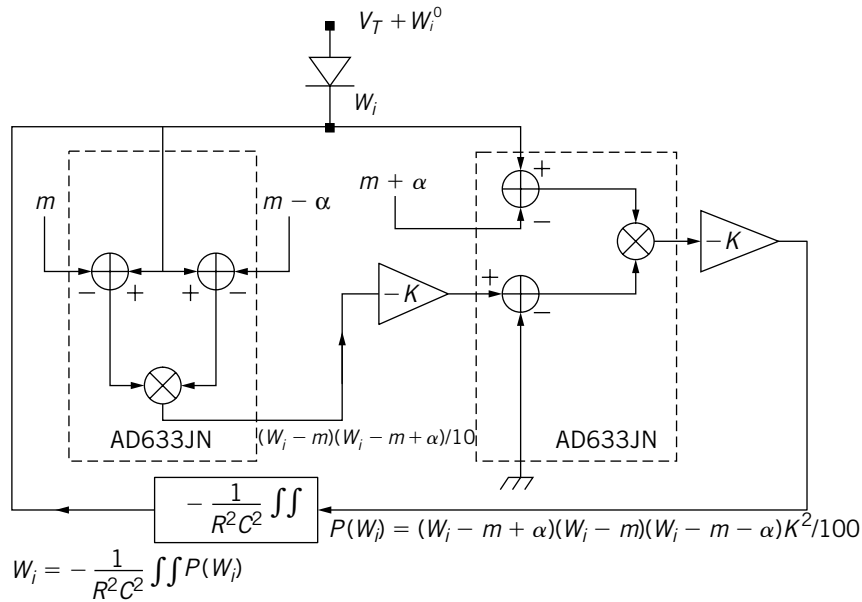$$W_i = -\frac{1}{R^2 C^2} \iint P(W_i)$$

FIGURE 13 Sketch of the elementary cell of the inertial system. m and α are adjusted with external direct current sources, whereas $-K$ is the inverting amplifier gain obtained using *TL081CN* operational amplifier. The $1N4148$ diode allows introduction of the initial condition W_i^0.

W_i is given by

$$P(W_i) = \frac{K^2}{100}(W_i - m)(W_i - m - \alpha)(W_i - m + \alpha), \qquad (24)$$

where the roots m, $m - \alpha$, $m + \alpha$ of the polynomial circuit are set with three different external direct current (DC) sources. As shown in Figure 14, the experimental characteristic of the nonlinear source is then in perfect agreement with its theoretical cubic law [Eq. (24)].

Next, a feedback between the input/output of the nonlinear circuits is ensured by a double integrator with time constant RC such that

$$W = -\frac{K^2}{100R^2C^2} \int \int (W_i - m + \alpha)(W_i - m - \alpha)(W_i - m)dt. \qquad (25)$$

Deriving Eq. (25) twice, the voltage W_i at the input of the nonlinear circuit is written as

$$\frac{d^2W_i}{dt^2} = -\frac{K^2}{100R^2C^2}(W_i - m + \alpha)(W_i - m - \alpha)(W_i - m), \qquad (26)$$

AQ5

which corresponds exactly to the equation of the purely inertial system (13) with
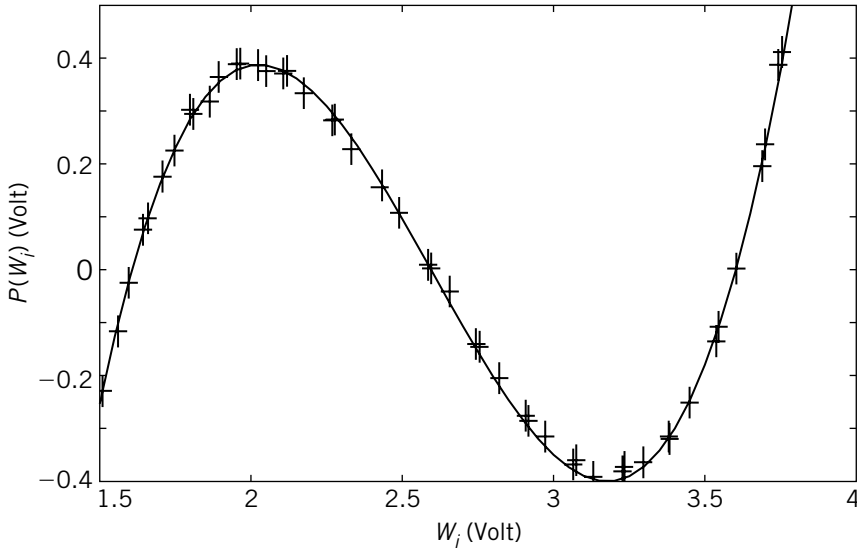
$$\omega_0 = K/(10RC). \qquad (27)$$

FIGURE 14 Theoretical cubic law in Eq. (24) in solid line compared to the experimental characteristic plotted with crosses. Parameters: $m = 2.58$ V, $\alpha = 1.02$ V, $K = 10$.

Finally, the initial condition W_i^0 is applied to the elementary cell via a 1N4148 diode with threshold voltage $V_T = 0.7\,V$. We adjust the diode anode potential to $W_i^0 + V_T$ with an external DC source with the diode cathode potential initially set to W_i^0. Then, according to Section III, the circuit begins to oscillate in the range $[W_i^0; 2m - W_i^0]$, while the potential of the diode anode remains $V_T + W_i^0$. Assuming that $m > W_i^0/2$, which is the case in our experiments, the diode is instantaneously blocked once the initial condition is introduced. Note that using a diode to set the initial condition presents the main advantage to "balance" the effect of dissipation inherent in electronic devices. Indeed, the intrinsic dissipation of the experiments tends to reduce the amplitude of the oscillations W_i^0. As soon as the potential of the diode cathode is below W_i^0, the diode conducts instantaneously, introducing periodically the same initial condition in the elementary cell. Therefore, the switch between the two states of the diode presents the advantage of refreshing the oscillation amplitude to their natural value as in absence of dissipation.

In summary, the oscillations are available at the diode cathode and are represented in Figure 15a for two different initial conditions, namely, $W_1^0 = 0\,V$ (top panel) and $W_2^0 = 0.2\,V$ (bottom panel). As previously explained, the way to introduce the initial condition allows balancing the dissipative effects since the oscillation remains with the same amplitude, namely in the range $[0\,V;\ 5.34\,V]$ for the first oscillator with initial condition 0, and $[0.2\,V;\ 5.1\,V]$ for the second one. Moreover, these ranges match with fairly good agreement the theoretical predictions presented in Section II.B.2, that is $[0\,V;\ 5.16\,V]$ for the first oscillator and $[0.2\,V;\ 4.96\,V]$ for the second one. Figure 15a also reveals that the two oscillators quickly achieve a phase opposition at the optimal time $t_{opt} = 1.46\,ms$ instead of $1.64\,ms$ as theoretically established in Section II.B.2. The oscillations difference between the two oscillators in Figure 15b reaches local minima and maxima in agreement with the theoretical behavior observed in Section III. A maximum of $5.1\,V$ is obtained corresponding to the phase opposition $W_1(t_{opt}) = 0\,V$ and $W_2(t_{opt}) = 5.1\,V$. Therefore, the weak difference of initial conditions between the oscillators is strongly increased at the optimal time t_{opt}. Despite a slight discrepancy of 11% for the optimal time, mainly imputable to the component uncertainties, a purely inertial nonlinear system is then implemented with the properties of Section III.

To perfectly characterize the experimental device, we now focus on the response of the nonlinear system to different initial conditions in the range $[0\,V;\ 0.2\,V]$. The plot of the voltage reached at the optimal time $t_{opt} = 1.46\,ms$ versus the initial condition is compared in Figure 16 to the theoretical curve obtained for the optimum time defined in Section II.B.2, namely, $1.64\,ms$. The experimental response of the system is
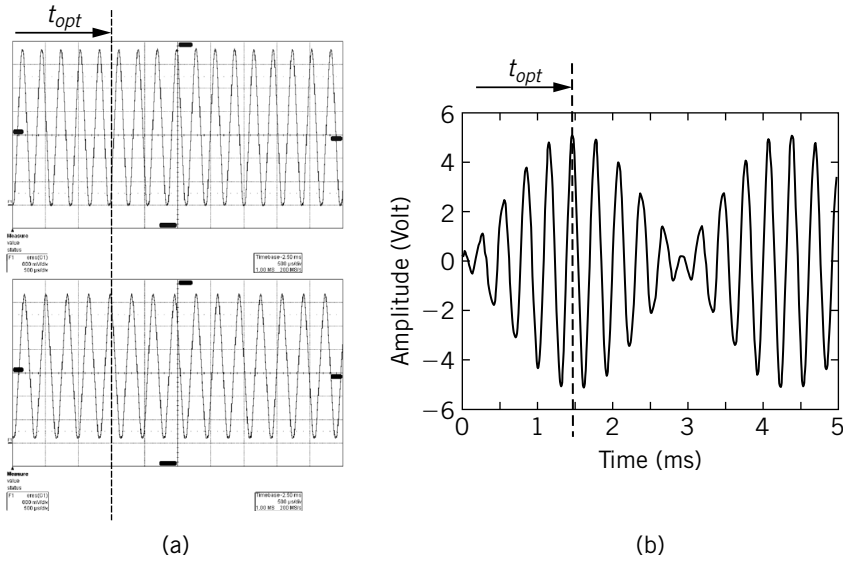
AQ6

(a)   (b)

FIGURE 15   (a): Temporal evolution of two elementary cells of the chain with respective initial conditions $W_1^0 = 0\,V$ (top panel) and $W_2^0 = 0.2\,V$ (bottom panel). (b): Evolution of the voltage difference between the two oscillators. Parameters: $K = 10$, $R = 10\,K\Omega$, $C = 10\,nF$, $m = 2.58\,V$, $\alpha = 1.02\,V$, $t_{opt} = 1.46\,ms$.
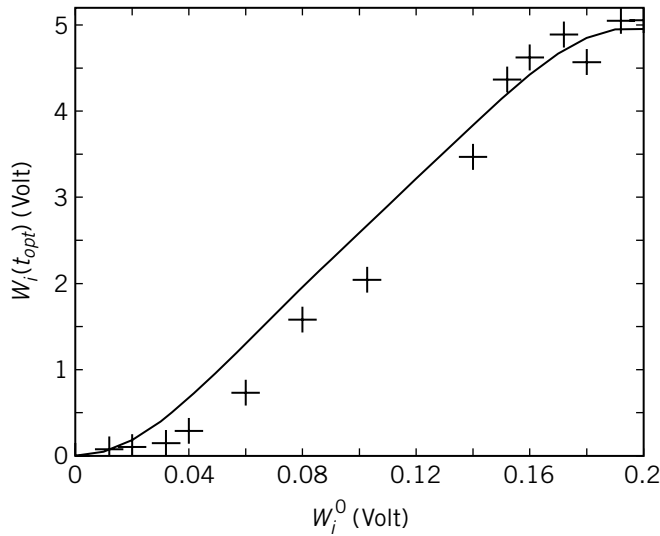

FIGURE 16   Response of the system to a set of initial conditions $W_i^0 \in [0;\ 0.2]$ at the optimal time. The solid line is obtained with Eqs. (20), (21), and (27) setting the time to the theoretical optimal value 1.64 ms, the initial condition varying in $[0;\ 0.2\,V]$. The crosses are obtained experimentally for the corresponding optimal time 1.46 ms. Parameters: $R = 10\,K\Omega$, $C = 10\,nF$, $m = 2.58\,V$, $\alpha = 1.02\,V$, $K = 10$.

then qualitatively confirmed by the theoretical predictions, which allows establishing the validity of the experimental elementary cell for the contrast enhancement presented in Section III.A.1.   AQ7

Finally, we also propose to investigate the response of the system after the optimum time, since it allows the extraction of gray levels. In order to enhance the measures accuracy, we extend the range of initial conditions to $[0, 0.5\,V]$ instead of $[0, 0.2\,V]$. The corresponding experimental optimal time becomes $t_{opt} = 564\,\mu s$, whereas the theoretical ones, deduced with the methodology in Section II.B.2, is $610\,\mu s$. The resulting theoretical and experimental responses are then plotted in Figure 17a, where a better agreement is effectively observed compared to Figure 16.
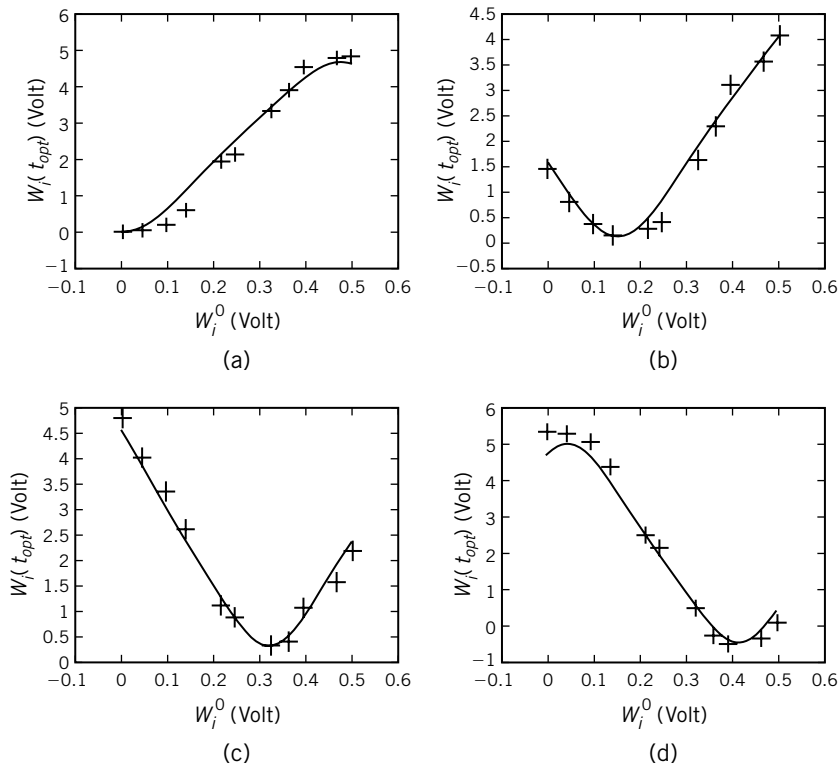

FIGURE 17   Theoretical response of the purely inertial system (solid line) compared to the experimental ones (crosses) for 4 different times and for a range of initial conditions $[0;\ 0.5\,V]$. Parameters: $R = 10\,K\Omega$, $C = 10\,nF$, $m = 2.58\,V$, $\alpha = 1.02\,V$, $K = 10$. (a) Experimental time $t = 564\,\mu s$ corresponding to the theoretical time $t = 610\,\mu s$. (b) Experimental time $t = 610\,\mu s$ and theoretical time $713\,\mu s$. (c) Experimental time $t = 675\,\mu s$ and theoretical time $789\,\mu s$. (d) Experimental time $t = 720\,\mu s$ and theoretical time $841\,\mu s$.

We have also reported the experimental device response for three different times beyond the optimal time $t_{opt} = 564\,\mu s$ in Figure 17b, c, and d—namely, for the experimental times $t = 610\,\mu s$, $t = 675\,\mu s$, and $t = 720\,\mu s$. Since a time scale factor $610/564 = 1.1684$ exists between the experimental and the theoretical optimal time, we apply this scale factor to the three previous experimental times. It provides the theoretical times $713\,\mu s$, $789\,\mu s$, and $841\,\mu s$. For each of these three times, we can then compare the experimental response to the theoretical one deduced by letting the initial condition vary in $[0;\ 0.5\,V]$ in Eqs. (20), (21), and (27). Despite some slight discrepancies, the behavior of the experimental device is in good agreement with the theoretical response of the system for the three processing times exceeding the optimal time. Therefore, the extraction of gray levels, presented in Section III.A.2, is electronically implemented with this elementary cell.

IV. REACTION-DIFFUSION SYSTEMS

A. One-Dimensional Lattice

The motion Eq. (4) of the nonlinear mechanical chain can also describe the evolution of the voltage at the nodes of a nonlinear electrical lattice. This section is devoted to the presentation of this nonlinear electrical lattice.

The nonlinear lattice is realized by coupling elementary cells with linear resistors R according to the principle of Figure 18a. Each elementary cell consists of a linear capacitor C in parallel with a nonlinear resistor whose current-voltage characteristic obey the cubic law

$$I_{NL}(u) = \beta u(u - V_a)(u - V_b)/(R_0 V_a V_b), \qquad (28)$$

where $0 < V_a < V_b$ are two voltages, β is a constant, and R_0 is the analog to a weighting resistor.
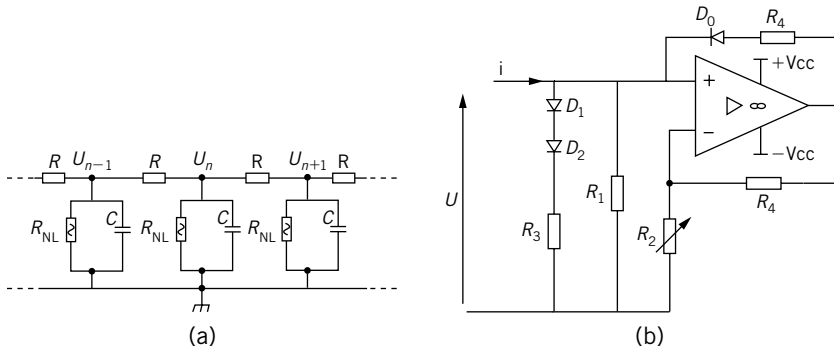

FIGURE 18   (a) Nonlinear electrical lattice. (b) The nonlinear resistor R_{NL}.
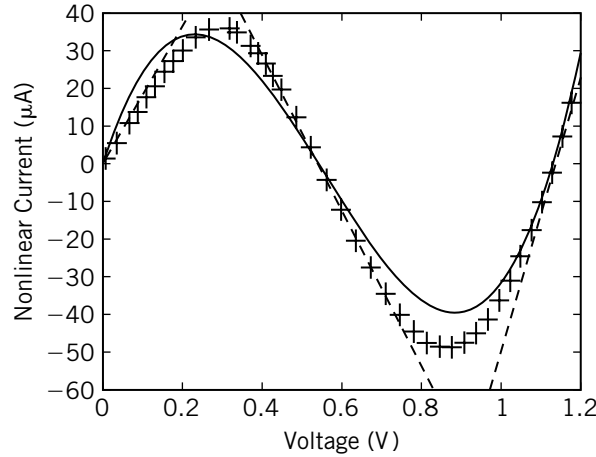
FIGURE 19   Current-voltage characteristics of the nonlinear resistor. The theoretical law [Eq. (28)] in the solid line is compared to the experimental data plotted with crosses. The dotted lines represent the asymptotic behavior of the nonlinear resistor. Parameters: $R_0 = 3.078\ K\Omega$, $V_b = 1.12\ V$, $V_a = 0.545\ V$, $\beta = 1$.

The nonlinear resistor can be developed using two different methods. The first method to obtain a cubic current is to consider the circuit of Figure 18b with three branches (Binczak *et al.*, 1998; Comte, 1996). A linear resistor R_3, a negative resistor, and another linear resistor R_1 are successively added in parallel thanks to $1N4148$ diodes. Due to the switch of the diodes, the experimental current-voltage characteristic of Figure 19 asymptotically displays a piecewise linear behavior with successively a positive slope, a negative one, and finally a positive one.

This piecewise linear characteristics is compared to the cubic law [Eq. (28)], which presents the same roots V_a, V_b, and 0 but also the same area below the characteristic between 0 and V_a. This last conditions leads to $\beta = 1$ and $R_0 = 3.078\ K\Omega$ (Morfu, 2002c).

An alternative way to realize a perfect cubic nonlinear current is to use a nonlinear voltage source that provides a nonlinear voltage $P(u) = \beta u(u - V_a)(u - V_b)/(V_a V_b) + u$ as shown in Figure 20 (Comte and Marquié, 2003).

This polynomial voltage is realized with *AD633JNZ* multipliers and classical *TL081CN* operational amplifiers. A resistor R_0 ensures a feedback between the input/output of the nonlinear source such that Ohm's law applied to R_0 corresponds to the cubic current in Eq. (28):

$$\frac{P(u) - u}{R_0} = I_{NL}(u). \tag{29}$$

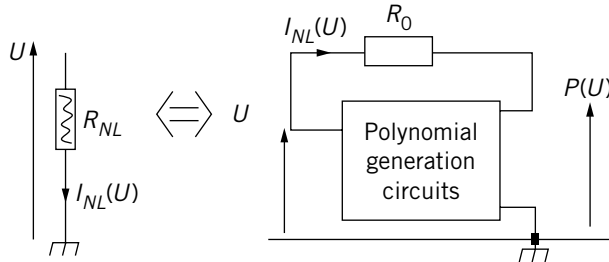As shown in Figure 21, this second method gives a better agreement with the theoretical cubic law [Eq. (28)].

FIGURE 20   Realization of a nonlinear resistor with a polynomial generation circuit.
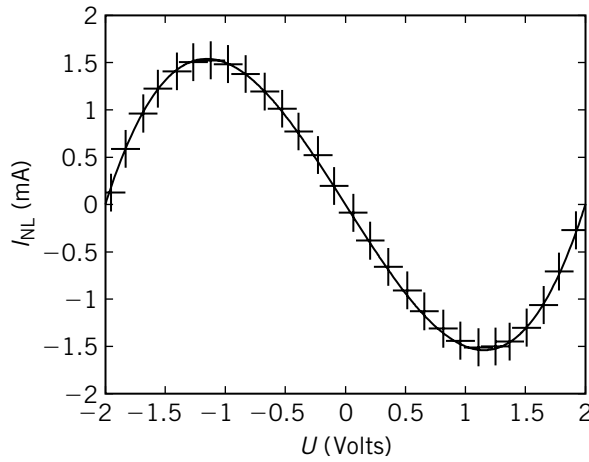$\beta = 10 V_a V_b$.

FIGURE 21   Current-voltage characteristics of the nonlinear resistor of Figure 20.
Parameters: $\beta = -10\, V_a V_b$, $V_a = -2\, V$, $V_b = 2\, V$.

Applying Kirchhoff's laws, the voltage U_n at the nth node of the lattice
can be written as

$$C\frac{dU_n}{d\tau} = \frac{1}{R}\big(U_{n+1} + U_{n-1} - 2U_n\big) - I_{NL}(U_n), \qquad (30)$$

where τ denotes the experimental time and $n = 1 \ldots N$ represents the node
number of the lattice.

Moreover, we assume zero-flux or Neumann boundary conditions,
which involves for $n = 1$ and $n = N$, respectively,

$$C\frac{dU_1}{d\tau} = \frac{1}{R}\big(U_2 - U_1\big) - I_{NL}(U_1), \qquad (31)$$

$$C\frac{dU_N}{d\tau} = \frac{1}{R}\big(U_{N-1} - U_N\big) - I_{NL}(U_N). \qquad (32)$$

Next, introducing the transformations

$$W_n = \frac{U_n}{V_b}, \qquad D = \frac{R_0}{R}\alpha\beta, \qquad t = \frac{\tau}{R_0\alpha C\beta}, \tag{33}$$

yields the discrete Nagumo equation in its normalized form,

$$\frac{dW_n}{dt} = D\big(W_{n+1} + W_{n-1} - 2W_n\big) + f(W_n). \tag{34}$$

Therefore, an electronic implementation of the overdamped network presented in Section II.A is realized.

B. Noise Filtering of a One-Dimensional Signal

One of the most important problems in signal or image processing is removal of noise from coherent information. In this section, we develop the principle of nonlinear noise filtering inspired by the overdamped systems (Marquié *et al.*, 1998). In addition, using the electrical nonlinear network introduced in Section IV.A, we also present an electronic implementation of the filtering tasks.

1. Theoretical Analysis

To investigate the response of the overdamped network to a noisy signal loaded as an initial condition, we first consider the simple case of a constant signal with a sudden change of amplitude. Therefore, we study the discrete normalized Nagumo equation

$$\frac{dW_n}{dt} = D\big(W_{n+1} + W_{n-1} - 2W_n\big) + f(W_n), \tag{35}$$

with $f(W_n) = -W_n(W_n - \alpha)(W_n - 1)$ in the specific case $\alpha = 1/2$. Furthermore, the initial condition applied to the cell n is assumed to be uniform for all cells, except for the cell $N/2$, where a constant perturbation b^0 is added; namely:

$$W_n(t = 0) = V^0 \qquad \forall n \neq \frac{N}{2}$$
$$W_{N/2}(t = 0) = V^0 + b^0. \tag{36}$$

The solution of Eq. (35) to the initial condition in Eq. (36) can be expressed with the following form

$$W_n(t) = V_n(t) + \epsilon b_n(t). \tag{37}$$

Inserting Eq. (37) in Eq. (35), we collect the terms of order 0 and 1 in ϵ with the reductive perturbation methods to obtain the set of differential equations (Taniuti and Wei, 1968; Taniuti and Yajima, 1969):

$$\frac{dV_n}{dt} = D(V_{n+1} + V_{n-1} - 2V_n) + f(V_n) \tag{38}$$

$$\frac{db_n}{dt} = D(b_{n+1} + b_{n-1} - 2b_n) - (3V_n^2 - 2V_n(1+\alpha) + \alpha)b_n \tag{39}$$

Assuming that V_n is a slow variable, Eq. (38) reduces to

$$\frac{dV_n}{dt} = f(V_n), \tag{40}$$

which provides the response of the system to a uniform initial condition V^0 (see details in Appendix A):

$$V(t) = \frac{1}{2}\left(1 + \frac{V^0 - \frac{1}{2}}{\sqrt{(V^0 - \frac{1}{2})^2 - V^0(V^0 - 1)e^{-\frac{t}{2}}}}\right). \tag{41}$$

Next, to determine the evolution of the additive perturbation, it is convenient to consider a perturbation under the following form:

$$b_n(t) = I_n(2Dt)g(t), \tag{42}$$

where I_n is the modified Bessel function of order n (Abramowitz and Stegun, 1970). Substituting Eq. (42) in Eq. (39), and using the property of the modified Bessel function,

$$\frac{dI_n(2Dt)}{dt} = D(I_{n+1} + I_{n-1}), \tag{43}$$

we obtain straightforwardly

$$\frac{dg}{dt} = -2Dg - \left[3V_n^2 - 2V_n(1-\alpha) + \alpha\right]g, \tag{44}$$

that is,

$$\frac{dg}{g} = -2Ddt - \left[3V_n^2 - 2V_n(1-\alpha) + \alpha\right]dt. \tag{45}$$

Noting that

$$\frac{df(V_n)}{dt} = -\left[3V_n^2 - 2V_n(1-\alpha) + \alpha\right]\frac{dV_n}{dt}, \tag{46}$$

and deriving Eq. (40) versus time, we derive

$$\frac{V_n''}{V_n'} = -\left[3V_n^2 - 2V_n(1-\alpha) + \alpha\right], \tag{47}$$

where V_n' and V_n'' denote the first and second derivative versus time.

Combining Eq. (47) and Eq. (45) allows expression of $g(t)$ as:

$$g(t) = Ke^{-2Dt}\frac{dV_n}{dt}, \tag{48}$$

where K is an integrating constant.

Deriving Eq. (41), we obtain $g(t)$ and thus the evolution of the perturbation:

$$b_n(t) = K\frac{I_n(2Dt)e^{-2Dt}e^{-t/2}}{8}\frac{V^0\left(V^0 - \frac{1}{2}\right)(V^0 - 1)}{\left[\left(V^0 - \frac{1}{2}\right)^2 - V^0(V^0-1)e^{-t/2}\right]^{3/2}}. \tag{49}$$

Writing $b_n(t=0) = b_n^0$ provides the value of the integrating constant K. The evolution of the perturbation $b_n(t)$ is then ruled by:

$$b_n(t) = \frac{b_n^0}{8}\frac{I_n(2Dt)e^{-2Dt}e^{-\frac{t}{2}}}{\left[\left(V_0 - \frac{1}{2}\right)^2 - V_0(V_0-1)e^{-\frac{t}{2}}\right]^{\frac{3}{2}}}. \tag{50}$$

Finally, in the case of multiple perturbations, the perturbation at the nth node of the lattice follows as

$$b_n(t) = \sum_{n'}\frac{b_{n'}^0}{8}\frac{I_{n'-n}(2Dt)e^{-2Dt}e^{-\frac{t}{2}}}{\left[\left(V_0 - \frac{1}{2}\right)^2 - V_0(V_0-1)e^{-\frac{t}{2}}\right]^{\frac{3}{2}}}, \tag{51}$$

where $I_{n'-n}$ is the modified Bessel function of order $n' - n$.

Eq. (41) shows that the evolution of the constant background does not depend on the coupling D. By contrast, Eq. (51) shows that the coupling D can be tuned to speed up the diffusion of the perturbation without affecting the constant background. Therefore, in signal-processing context, this property can be used to develop a noise filtering tool validate.

2. Theoretical and Numerical Results

In order to validate the theoretical analysis developed in Section IV.B.1, we have solved numerically Eq. (35) using a fourth-order Runge–Kutta algorithm with an integrating time step $dt = 10^{-3}$. Moreover, a uniform initial condition $V^0 = 0.4$ is loaded for all the $N = 48$ cells of the network except for the 24th cell. Indeed, for this cell, an additive perturbation $b^0 = 0.2$ is superimposed onto the constant background V^0 in order to match exactly the initial condition [Eq. (36)] considered in the theoretical Section IV.B.1.

We have investigated the evolution of both the constant background and the perturbation versus time. In Figure 22, the numerical results plotted with (•) signs match with perfect agreement the theoretical results predicted by Eqs. (41) and (51).

Moreover, the curve (*a*) of Figure 22 shows that the constant background given by Eq. (41) is unaffected by the nonlinear systems regardless of the coupling value D. By contrast, the behavior of the system for the
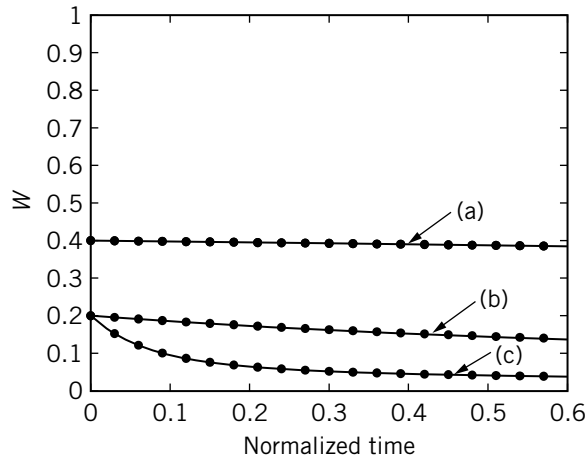

FIGURE 22   (a) Temporal evolution of a uniform initial condition $U^0 = 0.4$ applied to the entire network. (b) Temporal evolution of the perturbation applied to the cell $n = 24$ for $D = 0.5$ and $b^0 = 0.2$. (c) Temporal evolution of the perturbation applied to the cell $n = 24$ for $D = 5$ and $b^0 = 0.2$. Solid line: theoretical expressions of Eqs. (41) and (51); (•) signs: numerical results.

additive perturbation b^0 depends on the coupling parameter D (curves (*b*) and (*c*) in Figure 22). Indeed, for weak coupling values, namely, $D = 0.5$, the perturbation slowly decreases and seems to be quasi-unchanged, whereas for $D = 5$, the curve (*c*) exhibits a greater decreasing behavior. After time $t = 0.4$, the perturbation is significantly reduced for $D = 5$. Therefore, the coupling parameter D can be tuned to speed up the diffusion of the perturbation without disturbing the constant background. Furthermore, the time acts as a parameter that adjusts the filtering of the perturbation.

The state of the lattice for two different processing times is shown in Figure 23a and b for the previous coupling values, that is, $D = 5$ and $D = 0.5$, respectively. The initial perturbation represented in the dotted line (curve (*I*)) has almost disappeared for the specific value of the coupling $D = 5$ and for a processing time $t = 2$ (Figure 23a, curve (*III*)). As expected, curve (*III*) of Figure 23b shows that the perturbation is not filtered for $D = 0.5$ and for the same processing time $t = 2$. Furthermore, in both cases the constant background is slowly attracted by the nearest stable state—0 in our case.

Note that the spatiotemporal views of Figure 24 also reveal that the noise filtering is performed for $D = 5$ and a processing time $t = 2$.

Finally, to validate the processing task realized by the overdamped system, we propose to remove the noise from a more complex signal—a noisy sinusoïdal signal. The signal is first sampled with a total number of samples corresponding to the size of the overdamped network, namely, N. Next, a serial to parallel conversion is realized to load the N samples at the nodes of the 1D lattice. Therefore, we are led to consider the distribution of initial
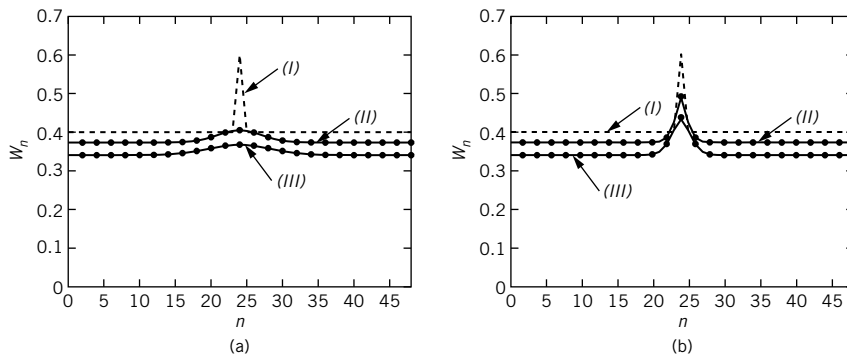

FIGURE 23   Response of the lattice to a uniform initial condition corrupted by a constant perturbation at two different processing times. (●) signs: numerical results; solid line: theoretical expression in Eq. (51). (a): $D = 5$; (b): $D = 0.5$. (*I*) initial condition for $t = 0$, (*II*) state of the lattice for $t = 1$, (*III*) state of the lattice for $t = 2$.
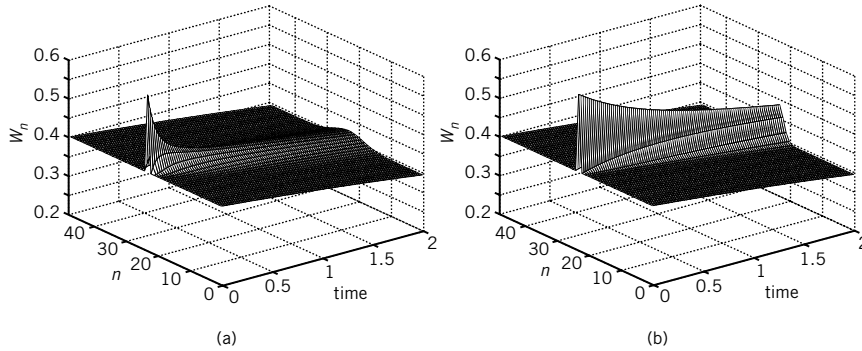
FIGURE 24 Spatiotemporal view of the response of the lattice to the previous initial condition. (a): $D = 5$; (b): $D = 0.5$.

conditions of Figure 25a in relation to

$$x_n = A \cos\left(2\pi \frac{2n}{N}\right) + \frac{1}{2} + \eta_n, \tag{52}$$

where η_n is a discrete white gaussian noise of root mean square RMS amplitude $\sigma = 0.15$. A and $2/N$ represent, respectively, the amplitude and the frequency of the coherent signal.

First we numerically investigate the response of the network with the coupling $D = 0.5$. As in the case of a constant background corrupted by a local perturbation, the system is unable to remove the noise from the sinusoidal signal for both processing times presented in Figure 25b and d. By contrast, for the favorable value of the coupling $D = 5$, the noise is completely filtered at the processing time $t = 1$ as shown in Figure 25e.

3. Experimental Results

To validate the electronic implementation of the nonlinear noise filtering tool, we consider the nonlinear electrical lattice introduced in Section IV.A with the nonlinear resistor of Figure 18b. In order to match the coupling value $D = 5$ and $D = 0.5$, the coupling resistor R is set to $R = 300\,\Omega$ and $R = 3\,K\Omega$, respectively. Moreover, all results are presented in normalized units using the transformation Eq. (33) to allow direct comparison with the theoretical analysis of Section IV.B.2. First, we experimentally report in Figure 26 the temporal evolution of the set of initial conditions consisting of a constant signal locally corrupted by a perturbation. As predicted in the theoretical section, the constant background is unaffected regardless of the coupling value (curve (*a*)), whereas when the coupling is adjusted
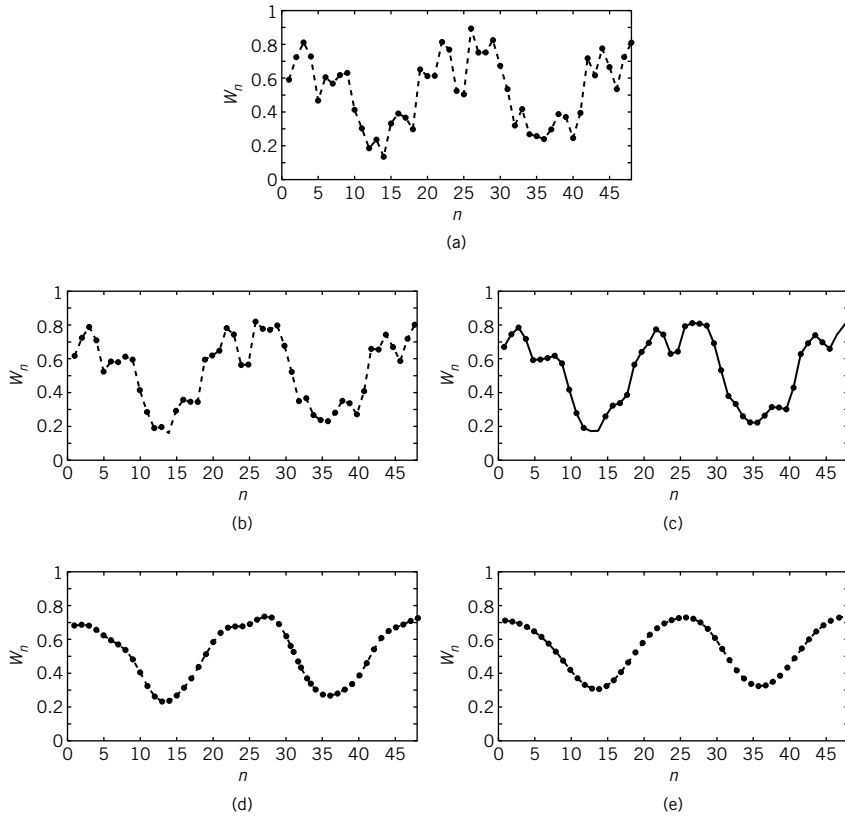
FIGURE 25   Noise filtering of a one-dimensional signal with an overdamped nonlinear network. (a): Noisy sinusoidal signal sampled and loaded as the initial condition at the nodes of the lattice. $\sigma = 0.15$, $N = 48$, and $A = 0.264$. (b), (c), (d), and (e) correspond to the filtered signal obtained for the following couples of processing time t and coupling D: (b) ($t = 0.4, D = 0.5$); (c) ($t = 1, D = 0.5$); (d) ($t = 0.4, D = 5$); (e) ($t = 1, D = 5$).

to its favorable value $D = 5$, the perturbation can be removed after a normalized processing time $t = 0.4$ (curve (c)). This result is also confirmed by the spatial response of the system at two different processing times. Indeed, as shown in Figure 27, the state of the lattice for $t = 2$ and $t = 4$ provides the signal without the perturbation only if the coupling D is chosen to equal 5.

Finally, we propose to filter the noisy sinusoidal signal of Figure 28a. After a processing time $t = 0.6$, the noise is completely removed for the coupling $D = 5$ (Figure 28c), which is not the case if the coupling is set to $D = 0.5$ (Figure 28b). Therefore, with a suitable choice of both processing time and resistor coupling, a noise filtering tool inspired by the
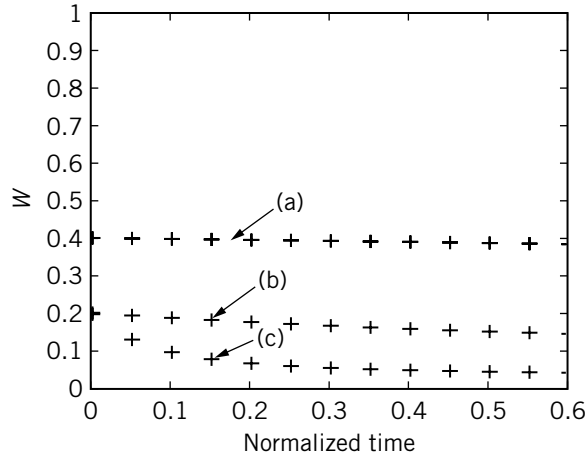
FIGURE 26   (a) Temporal evolution in normalized units of a uniform initial condition $W^0 = 0.4$ applied to the network. (b) Temporal evolution of the perturbation applied to the cell $n = 24$ for $b^0 = 0.2$ and $D = 0.5$ corresponding to a coupling resistor $R = 3\,K\Omega$. (c) Temporal evolution of the perturbation applied to the cell $n = 24$ for $b^0 = 0.2$ and $D = 5$ corresponding to a coupling resistor $R = 300\,\Omega$. $C = 33\,nF$. Nonlinearity parameters $\beta = 1$, $V_b = 1.12V$, $V_a = 0.545V$ involving $\alpha = 0.49$.
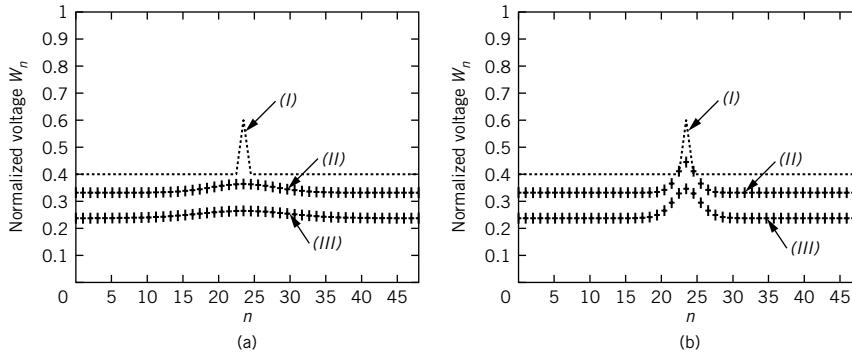

FIGURE 27   Response of the lattice to a uniform initial condition corrupted by a constant perturbation at two different processing times. Parameters: $C = 33\,nF$, $V_b = 1.12\,V$, $V_a = 0.545\,V$, $\alpha = 0.49$. (a): $R = 300\,\Omega$ that is $D = 5$; (b): $R = 3\,K\Omega$ that is $D = 0.5$. (I) initial condition for $t = 0$, (II) state of the lattice for $t = 2(\tau = 0.1$ ms), (III) state of the lattice for $t = 4$ ($\tau = 0.2$ ms).

properties of the nonlinear overdamped network is electronically implemented. Moreover, according to Eq. (33), the processing time could be adjusted by the value of the capacitor C to match real-time processing constraints.
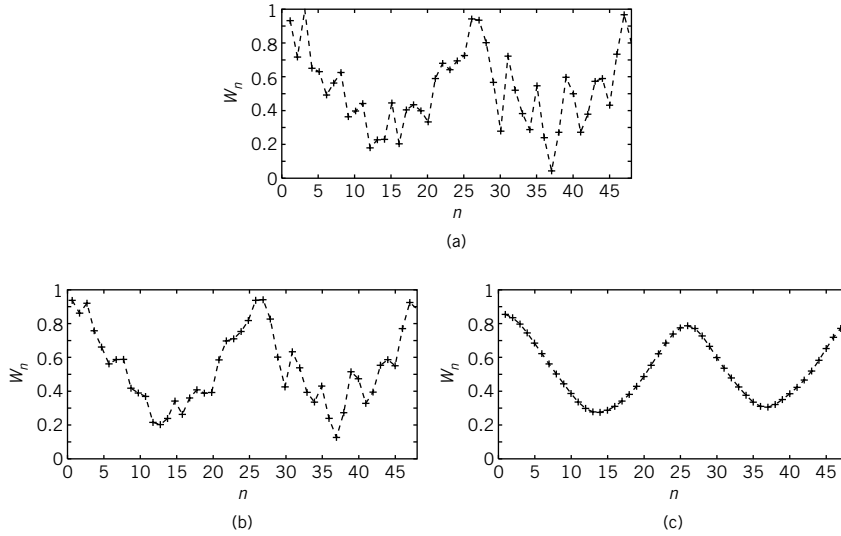
FIGURE 28   Noise filtering of a one-dimensional signal with an electrical nonlinear lattice. (a): Normalized noisy sinusoidal signal given by Eq. (52) loaded as initial condition at the nodes of the lattice. $\sigma = 0.15$, $N = 48$, and $A = 0.264$. (b): Filtered signal obtained for a processing time $t = 0.6$ ($\tau = 92.3\,\mu s$) and a coupling $D = 0.5$ (that is, $R = 3\,K\Omega$). (c): Filtered signal obtained for a processing time $t = 0.6$ ($\tau = 92.3\,\mu s$) and a coupling $D = 5$ (that is $R = 300\,\Omega$). Parameters: $C = 100\,nF$, $\beta = 1$, $V_b = 1.12\,V$, $V_a = 0.545\,V$.

C. Two-Dimensional Filtering: Image Processing

We now numerically extend the properties of the 1D lattice to a 2D network. Consider a CNN whose cell state $W_{i,j}$, representing the gray level of the pixel number i, j, follows the following set of equations:

$$\frac{dW_{i,j}}{dt} = f(W_{i,j}) + D \sum_{(k,l)\in Nr} \left(W_{k,l} - W_{i,j}\right), \quad i,j = 2 \ldots N-1, 2 \ldots M-1,$$
(53)

where $Nr = \{(i-1;j),(i+1,j),(i,j+1),(i,j-1)\}$ is the set of the four nearest neighbors, $N \times M$ the image size, and $f(W_{i,j})$ represents the non-linearity. The boundary conditions for the edges of the image express

$$\frac{dW_{1,j}}{dt} = f\left(W_{1,j}\right) + D\left(W_{1,j-1} + W_{2,j} + W_{1,j+1} - 3W_{1,j}\right), \, j = 2..M-1$$

$$\frac{dW_{N,j}}{dt} = f\left(W_{N,j}\right) + D\left(W_{N,j-1} + W_{N-1,j} + W_{N,j+1} - 3W_{N,j}\right),$$
$$j = 2..M-1$$

$$\frac{dW_{i,1}}{dt} = f(W_{i,1}) + D\big(W_{i-1,1} + W_{i+1,1} + W_{i,2} - 3W_{i,1}\big),\ i = 2..N-1$$

$$\frac{dW_{i,M}}{dt} = f(W_{i,M}) + D\big(W_{i-1,M} + W_{i+1,M} + W_{i,M-1} - 3W_{i,M}\big),$$

$$i = 2..N-1$$

while for the image corners, we consider the two nearest neighbors, that is

$$\frac{dW_{1,1}}{dt} = f(W_{1,1}) + D\big(W_{2,1} + W_{1,2} - 2W_{1,1}\big),$$

$$\frac{dW_{N,M}}{dt} = f(W_{N,M}) + D\big(W_{N,M-1} + W_{N-1,M} - 2W_{N,M}\big),$$

$$\frac{dW_{N,1}}{dt} = f(W_{N,1}) + D\big(W_{N-1,1} + W_{N,2} - 2W_{N,1}\big),$$

$$\frac{dW_{1,M}}{dt} = f(W_{1,M}) + D\big(W_{2,M} + W_{1,M-1} - 2W_{1,M}\big).$$

1. Noise Filtering

The initial condition applied to the cell i, j of the network corresponds to the initial gray level $W_{i,j}^0$ of the noisy image shown in Figure 29. The image after a processing time t is obtained noting the state $W_{i,j}(t)$ of all cells of the network at this specific time t (Comte *et al.*, 1998).

Figure 30 shows the filtered image obtained at the processing times $t = 1$, $t = 3$, $t = 6$, $t = 9$ and for the coupling values $D = 0.075$, $D = 0.1$, $D = 0.2$, and $D = 0.3$, respectively. The bistable behavior of the system established in Section II.A.1 involves a natural evolution of the image toward the two stable states of the system—0 and 1. Thus, as time increases, the image evolves into a black-and-white pattern. Therefore, to achieve correct noise filtering, the coupling parameter and the processing time must be adjusted.
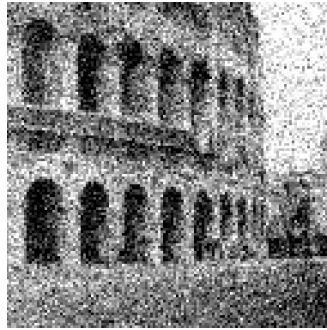
FIGURE 29   Noisy image of the Coliseum.

(a) (b) (c) (d)

(e) (f) (g) (h)

(i) (j) (k) (l)

(m) (n) (o) (p)
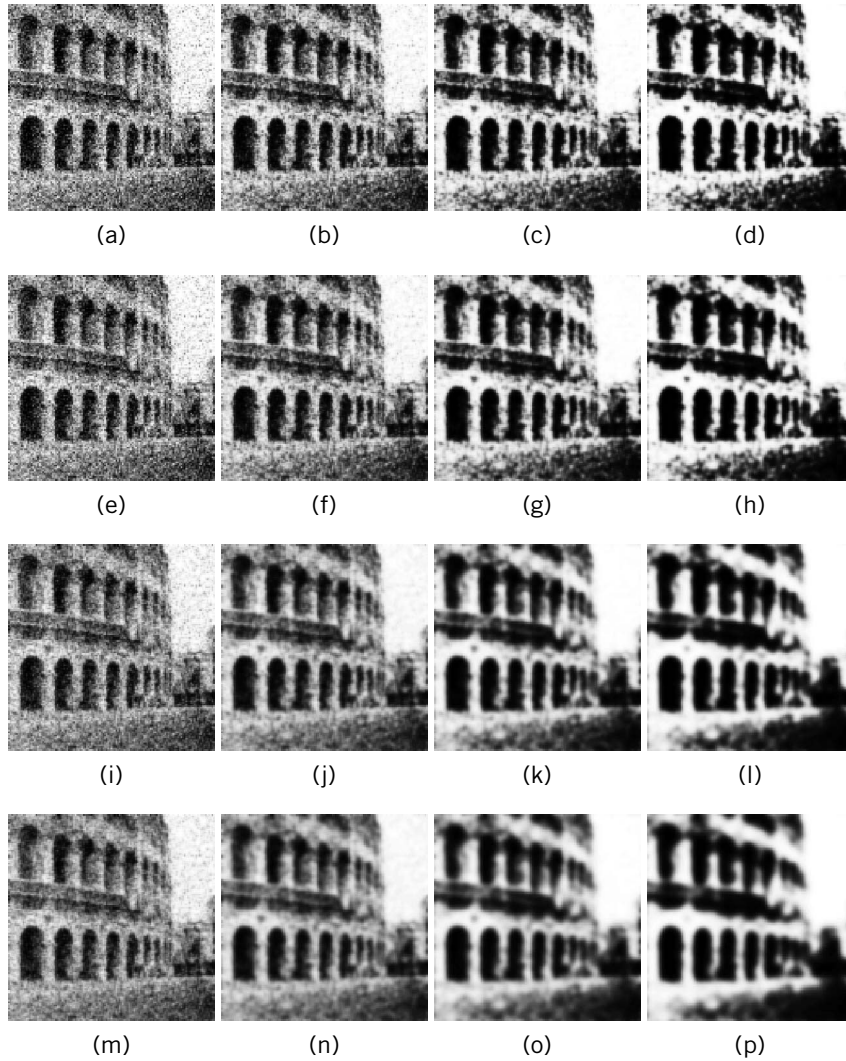
FIGURE 30 Noise filtering of the image represented in Figure 29. (a)−(d). Filtered image obtained for $D = 0.075$ and for the respective processing times $t = 1$, $t = 3$, $t = 6$, and $t = 9$. (e)−(h). Filtered image obtained for $D = 0.1$ and for the respective processing times $t = 1$, $t = 3$, $t = 6$, and $t = 9$. (i)−(l). Filtered image obtained for $D = 0.2$ and for the respective processing times $t = 1$, $t = 3$, $t = 6$, and $t = 9$. (m)−(p). Filtered image obtained for $D = 0.3$ and for the respective processing times $t = 1$, $t = 3$, $t = 6$, and $t = 9$.

For the lowest coupling value $D = 0.075$, Figure 30 shows that the noise is not removed before the image is binarized. For the coupling parameter $D = 0.2$ and $D = 0.3$, even if the noise is quickly removed, the filtered image becomes blurred for $t = 6$ and $t = 9$ (Figure 30k, l, o, p). Therefore, these settings of the coupling parameter are inappropriate. In fact, Figure 30f and g shows the filtered image with the best setting of the coupling and processing time: a coupling $D = 0.1$ and the processing times $t = 3$ or $t = 6$. Indeed, the filtered images are neither blurred nor binarized. Moreover, the system not only removes the noise, it also enhances the contrast of the initial image.

2. Edge Filtering

Because of a strong relationship between edge and object recognition, edge detection constitutes one of the most important steps for image recognition. Indeed, scene information often can be interpreted because of the edges. Classical edge detection algorithms are based on a second-order local derivative operator (Gonzalez and Wintz, 1987), whereas nonlinear techniques of edge enhancement are inspired mainly by the properties of reaction-diffusion media (Chua and Yang, 1988; Rambidi *et al.*, 2002).

We propose a strategy of edge detection based on the propagation properties of the nonlinear diffusive medium (Comte *et al.*, 2001). The image loaded in the 2D network is the black-and-white picture Figure 31a.

We established in Section II.A.2 that a 1D lattice modeled by the Nagumo equation supports kink and anti-kink propagation owing to the bistable nature of the nonlinearity. Indeed, if the nonlinearity threshold parameter $\alpha < 1/2$, the stable state 1 propagates, while if $\alpha > 1/2$, the stable state 0 propagates. Therefore, extending this property to a 2D network allows calculation of either erosion for $\alpha > 1/2$ or dilation for $\alpha < 1/2$, which are basic mathematical morphology operations, commonly performed in image processing (Serra, 1986). Moreover, if the initial image is subtracted from the image obtained with the network obeying to Eq. (53), we can deduce the contours of the image after a processing time t. Figure 31b shows the contour of a black-and-white image and its profile obtained with this method. The profile of the contour shows that its resolution is ∼10 pixels, which is insufficient to allow good edge enhancement of a more complex image.

This poor resolution is mainly attributable to the spatial expansion of the kink that results from the initial condition loaded in the lattice. Since the kink expansion reduces with the coupling, a natural solution consists of lowering the coupling. Unfortunately, the existence of the propagation failure effect provides a lower bound of the coupling D^* and thus hinders contour detection with good resolution. An alternative solution can be developed by using a nonlinearity that eliminates the propagation failure effect. Indeed, it has been shown for dissipative media (Bressloff and
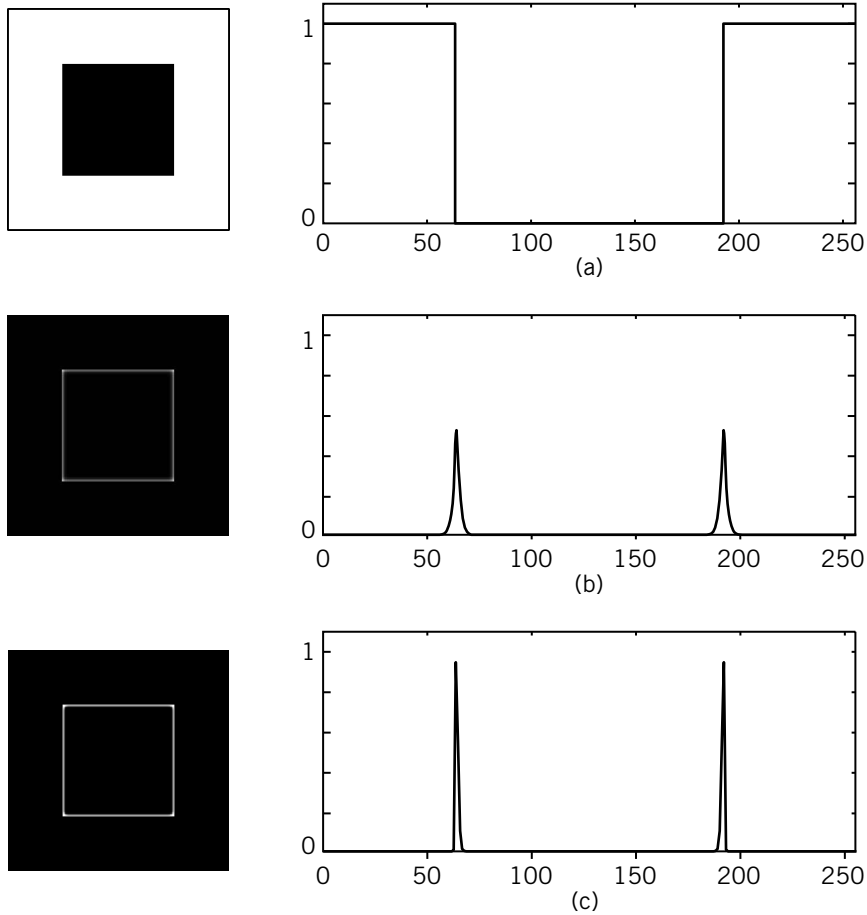
FIGURE 31   Contour detection of a black square in a white background. (a) Initial image and its profile. (b) Edge detection of the object and its profile obtained with the standard cubic nonlinearity [Eq. (5)] with threshold $\alpha = 1/3$. Processing time $t = 4$, $D = 1$. (c) Contour and the corresponding profile obtained with the nonlinearity [Eq. (54)]. Processing time $t = 4$, $D = 1$.

Rowlands, 1997) or for systems where both inertia and dissipation are taken into account (Comte *et al.*, 1999) that an inverse method allows definition of a nonlinear function for which exact discrete propagative kinks exist. Especially in the purely dissipative case, such function expresses

$$f(W_{i,j}) = D\epsilon\Big[(1 - a_2/2) - (a_0 W_{i,j} + a_1)^2\Big]$$
$$- \frac{Da_2(a_0 W_{i,j} + a_1)}{1 - (a_0 W_{i,j} + a_1)^2} + 2D(a_0 W_{i,j} + a_1), \quad (54)$$

where $\epsilon = 0.5$, $a_2 = 0.9$, $a_0 = 1.483$, and $a_1 = -0.742$ to ensure that the zeros of the nonlinearity remain $0, 1/3$, and 1. As expected, when this new nonlinearity is numerically implemented, the resolution of the detected contour in Figure 31c is reduced to 3 pixels.

Note that edge enhancement with the nonlinear overdamped network is not restricted to a black-and-white image. Indeed, the concept is based on the propagation properties of the system and can be extended to the case of an image with 256 gray levels. For instance, we propose to show numerically the contour enhancement of Figure 31a by considering the methodology used for the edge detection of the black-and-white picture.

The simulation results are summarized in Figure 32 for different processing times in the favorable case of the nonlinear function [Eq. (54)]. It is clear that again the time allows adjustment of the quality of the processing. Indeed, for processing times below $t = 1$, the edges of the image details are not revealed, whereas for processing times exceeding 1.33, the details begin to disappear. Furthermore, as times increases, the contours of the image are increasingly thinner owing to the propagation mechanism. The best contour enhancement is thus performed when the image details have not yet disappeared and when the enhanced contours remain sufficiently thin. In fact, this situation corresponds to the intermediate processing time $t = 1.33$ (Figure 32e).

3. Extraction of Regions of Interest

As explained in the previous subsections, in the case of cubic nonlinearity, a nonlinearity threshold $\alpha = 0.5$ allows noise filtering, while considering $\alpha \neq 0.5$ provides the contour of an image with poor resolution. Moreover, the nonlinearity $f(W)$ can be determined using an inverse method to optimize the filtering task. Therefore, the choice of the nonlinearity is of crucial interest in developing interesting and powerful image-processing tools. In this section, we go one step further by proposing a new nonlinearity to extract the regions of interest of an image representing the soldering between two rods of metal (Morfu *et al.*, 2007).

The noisy and weakly contrasted image of Figure 33 presents four regions of interest:

- First, the two rods of metal constitute the background of the image in light gray
- The stripe in medium gray at the center of the image represents the "soldered joint"
- A white spot corresponds to a "projection" of metal occurring during the soldering of the two rods of metal
- A dark gray spot represents a gaseous inclusion inside the soldering joint.

(a)

(b)   (c)   (d)

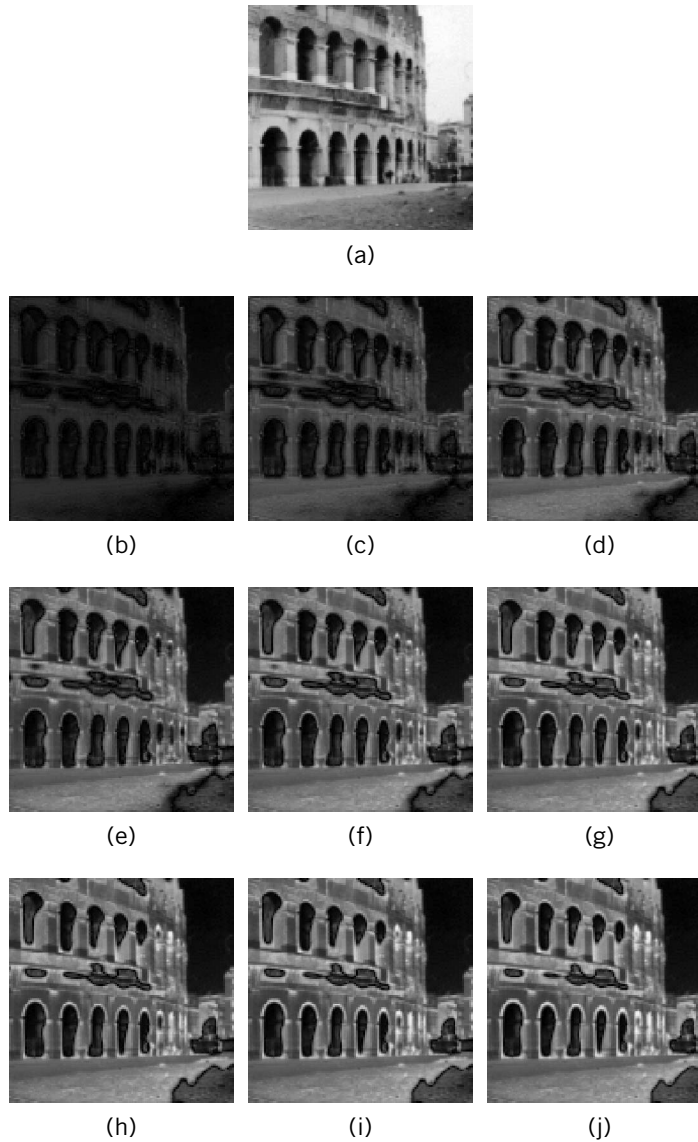(e)   (f)   (g)

(h)   (i)   (j)

FIGURE 32   Contour enhancement of a an image with 256 gray levels realized with the modified nonlinearity in Eq. (54). (a) Initial image. (b)−(j). Filtered image for the respective processing times $t = 0.33$, $t = 0.66$, $t = 1$, $t = 1.33$, $t = 1.66$, $t = 2$, $t = 2.33$, $t = 2.66$, and $t = 3$.
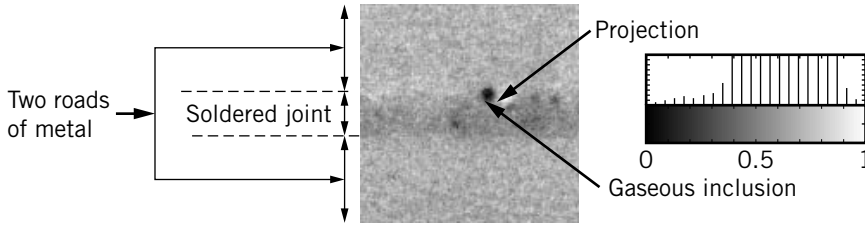
FIGURE 33 Noisy and weakly contrasted image of soldering between two rods of metal. The image histogram is represented at the right.
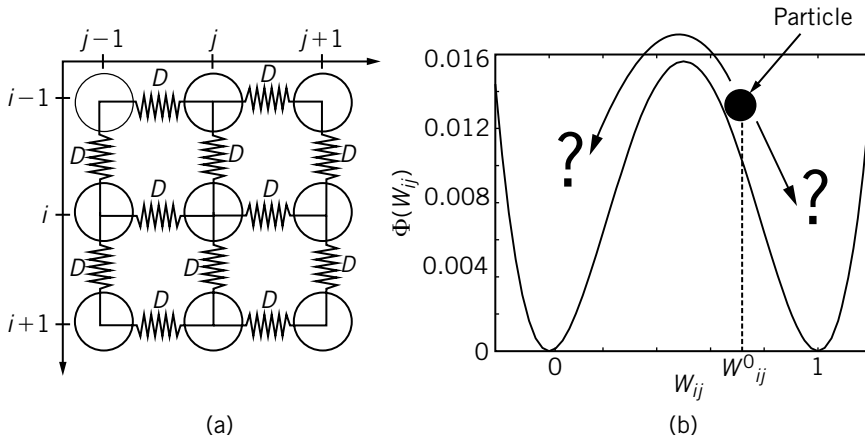

FIGURE 34 Mechanical point of view of the bistable overdamped network used for image processing. (a) The pixel with coordinates i,j and gray level $W_{i,j}$ is analog to an overdamped particle coupled by springs of strength D to its four nearest neighbors. (b) The particle is attracted in one of the two wells of the bistable potential according to the resulting elastic force applied by the four coupled particles.

a. Limit of the Bistable Network.   We first discuss the inability of the bistable overdamped network ruled by Eq. (53) to extract the four objects of the image. As explained in Section II.A.1, the bistability is ensured by using the cubic nonlinearity in Eq. (3). According to the mechanical description of the bistable system presented in Section II, a pixel of the image is analog to a particle experiencing a double-well potential $\phi(W) = -\int_0^W f(u)du$ and coupled to its four nearest neighbors by springs of strength D. As schematically shown in Figure 34, the particle with initial position $W_{i,j}^0$ is attracted in one of the two wells of potential depending on the competition between the resulting elastic force and the nonlinear force $f(W_{i,j})$.

$$D \sum_{(k,l)\in Nr} \left(W_{k,l} - W_{i,j} \right), \tag{55}$$

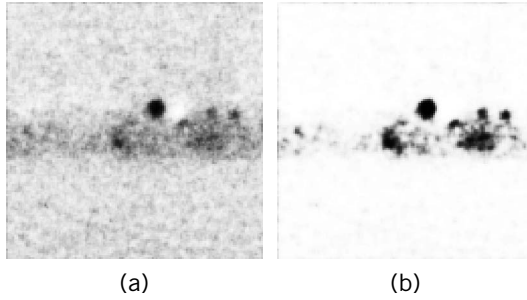(a)   (b)   (c)

FIGURE 35 Filtered images obtained with the bistable overdamped network described by Eqs. (3) and (53) in the case $\alpha = 1/2$. Coupling parameter: $D = 0.05$. Processing times: (a) $t = 4$; (b) $t = 10$; (c) $t = 3000$.

This property of the system allows sufficiently large time, the network is organized near the two stable states set by the nonlinearity, namely, 0 and 1. In image-processing context, it means that the resulting filtered image tends to be an almost black-and-white pattern. Figure 35 confirms this evolution of the filtered image versus the processing time since, when a cubic non-linearity is considered, a quasi – black-and-white image is obtained at the time $t = 3000$ (Figure 35c).

Note that for none of the proposed processing times was the bistable system able to properly remove the noise and to enhance the contrast of the regions of interest. Indeed, for $t = 4$ the noise is reduced but the details of the image begin to disappear (Figure 35a). In particular the projection is merged into the background for $t = 10$, indicating that the bistable nature of the system destroys the coherent information of the initial image (Figure 35b). Therefore, the inability of the overdamped system to extract the regions of interest is directly related to the bistable nonlinear force $f(W)$.

b. The Multistable Network.   To solve this problem and to maintain the coherent structure of the image, we introduce a nonlinearity with a multistable behavior. For instance, the following nonlinear force

$$f(W) = -\beta(n-1)\sin\left[2\pi(n-1)W\right] \tag{56}$$

derives from a potential $\phi(W) = -\int_0^W f(u)du$, which presents n wells and a potential barrier height between two consecutive potential extrema defined by β/π. This potential is represented in Figure 36 in the case of $n = 5$ wells of potential.

The multistable behavior of the network obeying to Eq. (53) with the sinusoidal force in Eq. (56) can be established by considering the uncoupled case.
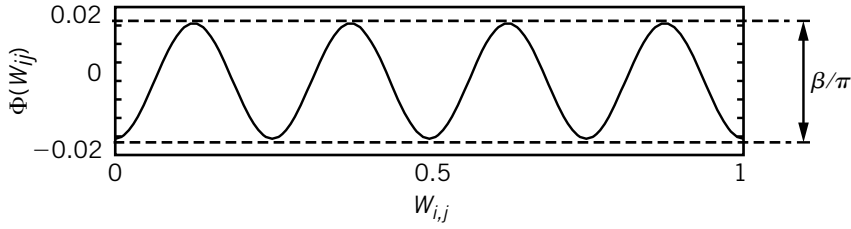
FIGURE 36   Multistable potential represented for $\beta = 9.82 \times 10^{-2}$ and $n = 5$. The potential barrier between two consecutive extrema is β/π.

Setting $D = 0$ in Eq. (53), we obtain

$$\frac{dW_{i,j}}{dt} = -\beta(n-1)\sin\left[2\pi(n-1)W_{i,j}\right]. \tag{57}$$

The stability analysis of the system can be performed with the methodology developed in Section II.A.1 by considering the roots of the sinusoidal force in Eq. (56). According to the sign of the derivative of the sinusoidal force, we can straightforwardly deduce that the unstable steady states of the system are given by

$$W_{thk} = (2k+1)/(2(n-1)) \qquad \text{with} \qquad k \in \mathbb{Z}, \tag{58}$$

while the stable steady states are defined by

$$W_k^* = k/(n-1) \qquad \text{with} \qquad k \in \mathbb{Z}. \tag{59}$$

Eq. (57) is solved in Appendix C to provide the temporal evolution of an overdamped particle experiencing the multistable potential of Figure 36 in the uncoupled case.

If k denotes the nearest integer of $(n-1)W_{i,j}^0$, and $W_{i,j}^0$ the initial position of the particle, the displacement $W_{i,j}(t)$ of the particle is expressed as

$$W_{i,j}(t) = \frac{1}{\pi(n-1)}\left[\arctan\left(\tan\left(\pi(n-1)W_{i,j}^0\right)e^{-\beta(n-1)^2 2\pi t}\right)\right] + \frac{k}{n-1}. \tag{60}$$

The multistable behaviour of the system is illustrated in Figure 37, which shows the temporal evolution of a particle submitted to different initial conditions in the range [0; 1]. It is clear that the unstable steady states of the system W_{thk} act as thresholds, while the stable steady states W_k^* correspond to attractors. Indeed, the final state of the
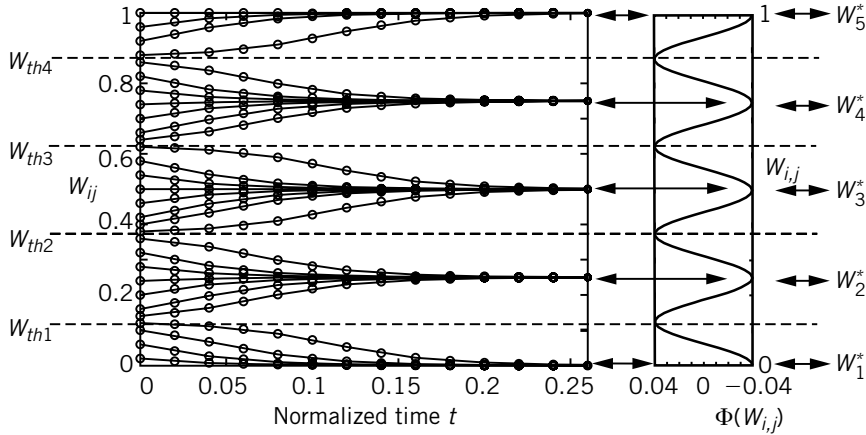
FIGURE 37 Temporal evolution of an overdamped particle experiencing the multistable potential. Parameters: $n = 5$ and $\beta = 0.25$. Solid line: theoretical expression of Eq. (60); open circles: numerical results obtained solving Eq. (57).

particle depends on the value of the initial condition compared to the thresholds W_{thk}. In particular if we neglect the transient, the asymp- AQ9 totic behavior of the uncoupled network is reduced to the following rules

$$ if \ \frac{2k - 1}{2(n - 1)} < W_{i,j}^0 < \frac{2k + 1}{2(n - 1)} \qquad W_{i,j}(t \mapsto +\infty) = \frac{k}{(n - 1)}. \tag{61} $$

Therefore, the asymptotic functioning [Eq. (61)] of the uncoupled network proves the multistable behavior of the system.

We now numerically use this multistable feature to extract the regions of interest of the image. In the coupled case, a pixel with initial gray level $W_{i,j}^0$ can take one of the n possible stable states according to the competition between the sinusoidal force and the resulting elastic force. The specific case $n = 5$ is shown numerically in Figure 38.

Unlike the bistable network, the noise is quickly removed without disturbing the coherent structure of the image consisting of "the projection," "the gaseous inclusion," "the background," and the "soldered joint" (Figure 38a for $t = 0.2$ and (b) for $t = 2$). Next, for a sufficiently longer time, namely $t = 5000$, the image no longer evolves and each defect of the soldering appears with a different mean gray level corresponding to one of the five stable steady states of the system (Figure 38c). An extraction of the interest regions of the image is then performed with this overdamped network.
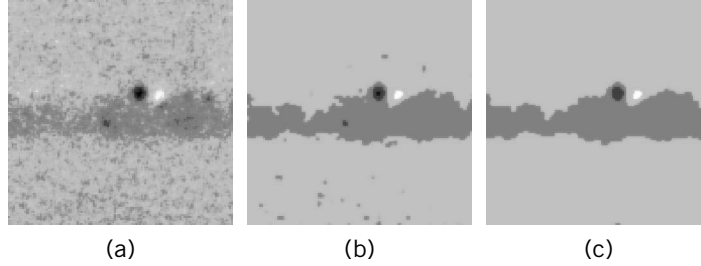
(a)   (b)   (c)

FIGURE 38   Filtered images obtained with the multistable overdamped network described by Eqs. (53) and (56). Nonlinearity parameters: $\beta = 9.82 \times 10^{-2}$, $n = 5$. Coupling parameter: $D = 1.6$. Processing times: (a) $t = 0.2$; (b) $t = 2$; (c) $t = 5000$.
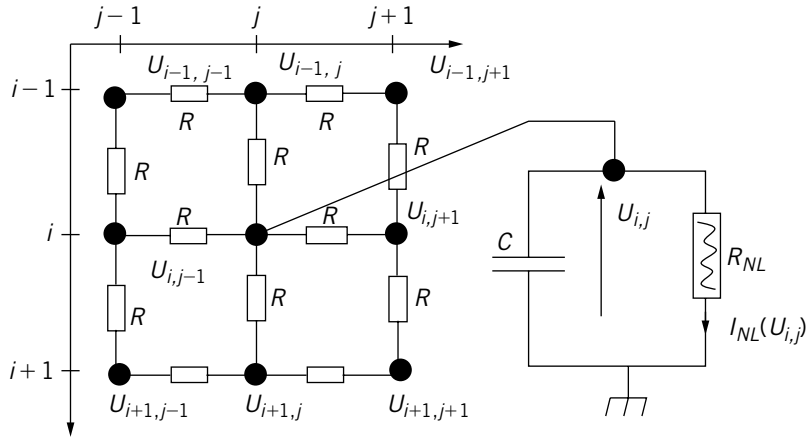
FIGURE 39   Electronic sketch of the multistable nonlinear network. R Represents the coupling resistor, C a capacitor, and R_{NL} a nonlinear resistor. INL denotes the nonlinear current and $U_{i,j}$ the voltage of the cell with coordinates i, j.

c. Electronic Implementation of the Multistable Network.   The electronic implementation of the multistable network is realized according to the methodology of Figure 39 by coupling elementary cells with linear resistors.

Each elementary cell includes a capacitor in parallel with a nonlinear resistor whose current-voltage characteristics can be approximated by the sinusoïdal law on the range $[-2V; 2V]$:

$$I_{NL}(U) \simeq I_M \sin(2\pi U). \tag{62}$$

The methodology in the Section IV.A to realize the cubic nonlinearity with a polynomial source can be used to obtain the sinusoidal law in Eq. (62). First, a least-square method at the order 15 allows us to fit the

sinusoidal expression in Eq. (62) by a polynomial law $P(U)$ in the range $[-2V; 2V]$. This provides the coefficients of the polynomial source $P(U)$ by generating the sinusoidal current

$$I_{NL}(U) = P(U)/R_0. \tag{63}$$

The experimental current-voltage characteristics is compared in Figure 40b to the theoretical expression in Eq. (62). The weak discrepancies observed between the theoretical and experimental laws can be reduced by increasing the order of the least-square method. However, enhancing the agreement with the sinusoidal law presents the main disadvantage to considerably increasing the number of electronic components used for the realization of the nonlinear resistor. Nevertheless, at the order 15, the experimental nonlinear current presents nine zeros and its derivative ensures the existence of five stable steady states and four unstable steady states. It is thus not of crucial interest to increase the order of the approximation, provided that the nonlinear resistor exhibits the multistability.
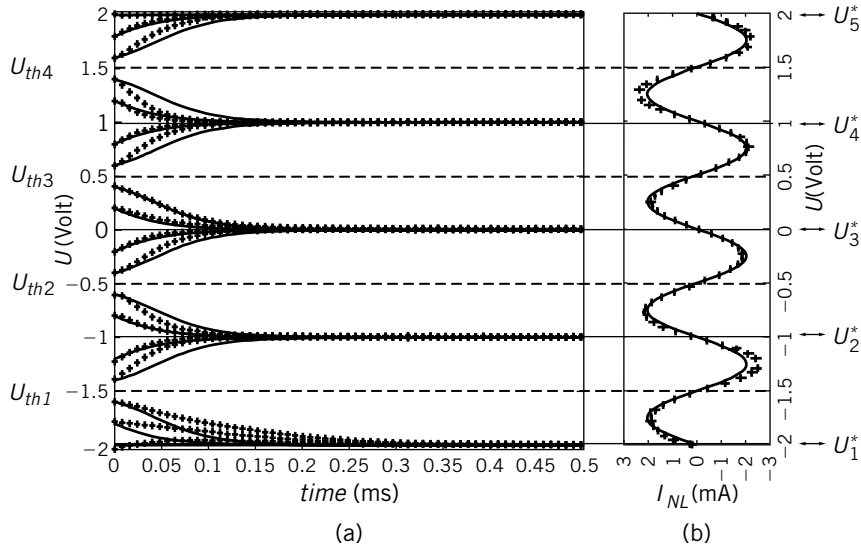
FIGURE 40 (a) Response of an elementary cell of the multistable network to different initial conditions in the uncoupled case. The plot of the theoretical expression [Eq. (60)] in the solid line is compared to the experimental results represented by crosses. (b) Nonlinear current-voltage characteristics. The sinusoidal law [Eq. (62)] in the solid line matches the experimental characteristics shown by plus sign (+). The component values are $R_0 = 2\,K\Omega$, $C = 390\,nF$, $I_M = 2mA$. The zeros of the sinusoidal current defines the four unstable states U_{th1}, U_{th2}, U_{th3}, and U_{th4}, which correspond to thresholds and the five stable steady states U_1^*, U_2^*, U_3^*, U_4^*, and U_5^*, which correspond to attractors.

Applying the Kirchhoff laws to the electrical network of Figure 39, we deduce the differential equation, which rules the evolution of the voltage $U_{i,j}$ at the nodes (i,j)

$$C\frac{dU_{i,j}}{d\tau} = -I_{NL}(U_{i,j}) + \frac{1}{R} \sum_{(k,l)\in Nr} (U_{k,l} - U_{i,j}). \qquad (64)$$

In Eq. (65), $Nr = \{(i;j-1), \ (i;j+1), \ (i-1;j), \ (i+1;j)\}$ denotes the neighborhood and τ represents the experimental time.

Next, the transformations

$$\tau = tR_0C, \ \beta = \frac{I_M R_0}{(n-1)^2}, \ U_{i,j} = W_{i,j}(n-1) - 2 \ \text{and} \ D = \frac{R_0}{R}, \quad (65)$$

lead to the normalized equation

$$\frac{dW_{i,j}}{dt} = \frac{P(W_{i,j}(n-1)-2)}{n-1} + D \sum_{(k,l)\in Nr} \left(W_{k,l} - W_{i,j}\right). \qquad (66)$$

The normalization is completed by noting that for $W_{i,j} \in [0; 1]$, that is, for $U_{i,j} \in [-2V; 2V]$,

$$P\left[W_{i,j}(n-1) - 2\right] = -R_0 I_{NL}\left[W_{i,j}(n-1) - 2\right]$$
$$\simeq -\beta(n-1)^2 \sin(2\pi(n-1)W_{i,j}). \qquad (67)$$

The experimental network described by Eq. (66) appears as an analog simulation of the normalized multistable network used for image processing.

Let us finally reveal the multistable behaviour of the elementary cell of the experimental network by investigating its response to different initial conditions in the uncoupled case. In addition, to allow a direct comparison with the theoretical expression (60), all the results are presented in normalized units in Figure 40a. First, we note that the component uncertainties does not explain the observed discrepancies. The poor correlation between the experimental results and the theoretical prediction is allocated to the nonlinearity provided by the nonlinear resistor, which does not exactly follow the sinusoidal law in Eq. (62). Nevertheless, the multistable property of the system is experimentally established. Indeed, there exist four threshold values, U_{th1}, U_{th2}, U_{th3}, and U_{th4} that allow determination of the final state of the elementary cell among the five possible stable steady states,

U_1^*, U_2^*, U_3^*, U_4^*, and U_5^*. Therefore, the image-processing task inspired by the multistable property of the system is implemented with the electronic device in Figure 39.

V. CONCLUSION

This chapter has reported a variety of image-processing operations   AQ10
inspired by the properties of nonlinear systems. Considering a mechanical analogy, we have split the class of nonlinear systems into purely inertial systems and overdamped systems. Using this original description, we have established the properties of nonlinear systems in the context of image processing.

For purely inertial systems, image-processing tasks such as contrast enhancement, image inversion, gray level extraction, or image encryption can be performed. The applications of the nonlinear techniques presented herein are similar to those developed by means of chemical active media (Teuscher and Adamatzky, 2005), even if these last media are rather overdamped than inertial. In particular, the dynamics of the nonlinear oscillators network, which enables contrast enhancement, can also be used to reveal "hidden images." Indeed, "hidden images" are defined as fragments of a picture with brightness very close to the brightness of the image background. Despite a weak difference of brightness between the hidden image and the image background, our nonlinear oscillators network take advantage of its properties to reveal the hidden image.

Another interesting property of this network is that is consecutively reveals fields of the image with increasing or decreasing brightness at different processing times. We trust that this feature, also shared by Belousov–Zhabotinsky chemical media, may have potential applications in image analysis in medicine (Teuscher and Adamatzky, 2005).

Finally, the noise effects in this purely inertial network lead to cryptography applications. Unlike classical cryptography devices, built with chaotic oscillators, we have proposed an encryption scheme based on the reversibility of our inertial system. Moreover, the encryption key, which ensures the restoration of the initial data, is the time of evolution of the data loaded in the nonlinear network. Therefore, the main advantage of our device is that it allow an easy change of the encryption key.

The properties of strongly dissipative or overdamped systems can also give rise to novel image-processing tools. For instance, we have shown the possibility of achieving noise filtering, edge detection, or extraction of regions of interest of a weakly contrasted picture. With regard to noise filtering applications based on reaction-diffusion media, the processing is based on the transient behavior of the network since the filtered image depends on the processing times. By contrast, the extraction of regions of

interest presents the main advantage of independence from the processing time since the filtering is realized when the network reaches a stationary pattern. Therefore, this feature can allow an automatic implementation of the processing task.

VI. OUTLOOKS

A. Outlooks on Microelectronic Implementation

For each nonlinear processing example, we have attempted to propose an electronic implementation using discrete electronic components. Even if these macroscopic realizations are far from real practical applications, they present the primary advantage of validating the concept of integration of CNN for future development in microelectronics.

Indeed, in recent years the market for solid-state image sensors has experienced explosive growth due to the increasing demands for mobile imaging systems, video cameras, surveillance, or biometrics. Improvements in this growing digital world continue with two primary image sensor technologies: charge coupled devices (CCD) and CMOS sensors. The continuous advances in CMOS technology for processors and DRAMs have made CMOS sensor arrays a viable alternative to the popular CCD sensors. New technologies provide the potential for integrating a significant amount of VLSI electronics into a single chip, greatly reducing the cost, power consumption, and size of the camera (Fossum, 1993; Fossum, 1997; Litwiller, 2001; Seitz, 2000). In past years, most research on complex CMOS systems has dealt with the integration of sensors providing a processing unit at chip level (*system-on-chip* approach) or at column level by integrating an array of processing elements dedicated to one or more columns (Acosta *et al.*, 2004; Kozlowski *et al.*, 2005; Sakakibara 2005; Yadid-Precht and Belenky, 2003). Indeed, pixel-level processing is generally dismissed because pixel sizes are often too large to be of practical use. However, as CMOS image sensors scale to 0.18-μm processes and below, integrating a processing element at each pixel or group of neighboring pixels becomes feasible. More significantly, using a processing element per pixel offers the opportunity to achieve massively parallel computations and thus the ability to implement full-image systems requiring significant processing such as digital cameras and computational sensors (El-Gamal *et al.*, 1999; Loinaz *et al.*, 1998; Smith *et al.*, 1998). The latest significant progress in CMOS technologies have made possible the realization of vision systems on chip (VSoCs). Such VSoCs are eventually targeted to integrate within a semiconductor substrate the functions of optical sensing, image processing in space and time, high-level processing, and the control of actuators. These chips consist of arrays of mixed-signal processing elements (PEs), which operate

AQ11

AQ12

in accordance with single-instruction multiple-data (SIMD) computing architectures.

The main challenge in designing a SIMD pixel parallel sensor array is the design of a compact, low-power but versatile and fully programmable processing element. For this purpose, the processing function can be based on the paradigm of CNNs. CNNs can be viewed as a very suitable framework for systematic design of image-processing chips (Roska and Rodriguez-Vazquez, 2000). The complete programmability of the interconnection strengths, its internal image-memories, and other additional features make this paradigm a powerful beginning for the realization of simple and medium-complexity artificial vision tasks (Espejo *et al.*, 1996). Some proof-of-concept chips operating on preloaded images have been designed (Czuni *et al.*, 2001; Rekeczky *et al.*, 1999). Only a few researchers have integrated CNN on real vision chips. As an example, Espejo (Espejo *et al.*, 1998) reports a 64×64-pixel programmable computational sensor based on a CNN. This chip is the first fully operational CNN vision-chip reported in the literature that combines the capabilities of image transduction, programmable image-processing, and algorithmic control on a common silicon substrate. It has successfully demonstrated operations such as low-pass image filtering, corner and border extraction, and motion detection. More recently, other studies have focused on the development of CMOS sensors including the CNN paradigm (Carmona *et al.*, 2003; Petras *et al.*, 2003). The chip consists of 1024 processing units arranged into a 32×32 grid and contains approximatively 500,000 transistors in a standard 0.5-μm CMOS technology. However, in these pioneering vision chips, the pixel size is often greater than $100\,\mu m \times 100\,\mu m$. Obviously, these dimensions cannot be considered as realistic dimensions for a real vision chip. A major part of this crucial problem should be resolved in future years by using the newly emerging CMOS technologies. Indeed, CMOS image sensors directly benefit from technology scaling by reducing pixel size, increasing resolution, and integrating more analog and digital functionalities on the same chip with the sensor. We expect that further scaling of CMOS image sensor technology and improvement in their imaging performances will eventually allow the implementation of efficient CNNs dedicated to nonlinear image processing.

B. Future Processing Applications

The nonlinear processing tools developed in this chapter are inherited from the properties of homogeneous media. In the case of applications based on the properties of reaction-diffusion media, it is interesting to consider the effects of both nonlinearity and structural inhomogeneities. Indeed, novel properties inspired by biological systems, which are inhomogeneous rather

than homogeneous (Keener, 2000; Morfu *et al.*, 2002a; Morfu *et al.*, 2002b; Morfu, 2003), could allow optimizing the filtering tools developed in this chapter.

For instance, in Section IV.C.1, the noise removal method based on the homogeneous Nagumo equation provides a blurry filtered image. In addition, it is difficult to extract the edge of the image with an accurate location. Indeed, noting that the contours of the image correspond to steplike profiles, the diffusive process increases the spatial expansion of the contours. To avoid this problem, anisotropic diffusion has been introduced to reduce the diffusive effect across the image contour. This method has been proposed by Perona and Malik (1990) to encourage intraregion smoothing in preference to interregion smoothing. To obtain this property, Perona and Malik replaced the classical linear isotropic diffusion equation

$$\frac{\partial I(x,y,t)}{\partial t} = div(\nabla I), \tag{68}$$

by

$$\frac{\partial I(x,y,t)}{\partial t} = div(g(\|\nabla I\|)\nabla I), \tag{69}$$

to adapt the diffusion with the image gradient. In Eqs. (68) and (69), $I(x,y,t)$ represents the brightness of the pixel located at the spatial position (x,y) for a processing time t, while $\|\nabla I\|$ is the gradient amplitude. Moreover, the anisotropy is ensured by the function $g(\|\nabla I\|)$ which "stops" the diffusion across the edges. For instance, Perona and Malik considered the function

$$g(x) = \frac{1}{1 + \frac{x^2}{K^2}}, \tag{70}$$

where K is a positive parameter.

Noting that when $x \mapsto \infty$, $g(x) \mapsto 0$, the effect of anisotropic diffusion is to smooth the original image while the contours are preserved. Indeed, the edge of the image corresponds to brightness discontinuities that lead to strong values of the image gradient (Black *et al.*, 1998). This interesting property of anisotropic diffusion is illustrated in Figure 41.

For sake of clarity, the algorithm developed by Perona and Malik is rather extensively detailed in Appendix D and we discuss here only the results obtained by filtering the noisy picture in Figure 41a. Contrary to the isotropic nonlinear diffusion based on the Nagumo equation, the edge of the image remains well localized for all the processing times presented
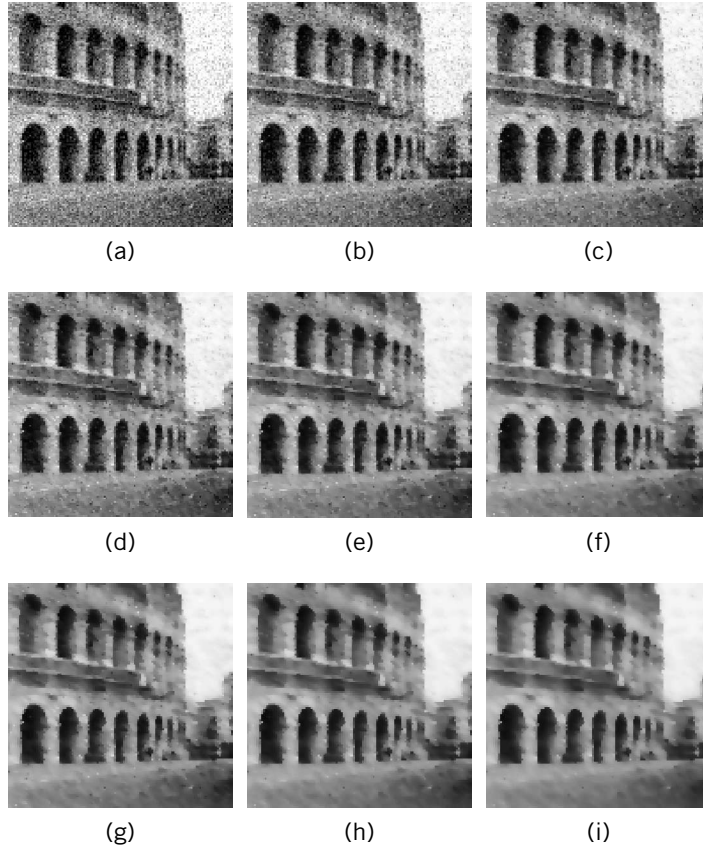
FIGURE 41 Noise filtering based on anisotropic diffusion. The filtering images are obtained using the algorithm detailed in Appendix D with the parameters $dt = 0.01$ and $K = 0.09$. (a) initial image, (b)−(i) images for the respective processing times $t = 1$, $t = 2$, $t = 3$, $t = 4$, $t = 5$, $t = 6$, $t = 7$, and $t = 8$.

in Figure 41. However, although the noise seems removed for processing times exceeding $t = 5$, the contrast of the image is never enhanced. Therefore, anisotropic diffusion and nonlinear diffusion do not share the same weakness and it could be interesting to attempt to circumvent the limitations of this two techniques.

For instance, if we compare the continuous Equation (9) of nonlinear diffusion with the anisotropic Equation (69) proposed by Perona and Malik, it is clear that the anisotropy can be introduced into our system via the coupling parameter D. Moreover, with Perona and Malik's method, the pixel brightness does not directly experience the nonlinearity as in our method. Therefore, the nonlinear noise filtering tool presented in Section IV.C.1 could be more efficient if the interesting properties of anisotropic

diffusion were also considered by introducing a coupling law. In particular we expect that the anisotropy preserves the location of the image edges, while the nonlinearity enhances the image contrast and removes the noise in the same time.

Finally, we close this chapter by presenting another interesting and nonintuitive phenomenon that occurs in nonlinear systems under certain conditions. This effect, known as the stochastic resonance (SR) effect was introduced in the 1980s to account for the periodicity of ice ages (Benzi *et al.*, 1982). Since then, the SR effect has been widely reported in a growing variety of nonlinear systems (Gammaitoni *et al.*, 1998), where it has been shown that adding an appropriate amount of noise to a coherent signal at a nonlinear system input enhances the response of the system. Detection of subthreshold signal using noise has been proven in neural information process (Longtin, 1993; Nozaki *et al.*, 1999; Stocks and Manella, 2001) and in data transmission fields (Barbay, *et al.*, 2001; Comte and Morfu, 2003; Duan and Abbott, 2005; Morfu *et al.*, 2003; Zozar and Amblard, 2003), as well as information transmission in array such as a stochastic resonator (Báscones *et al.*, 2002; Chapeau-Blondeau, 1999; Lindner *et al.*, 1998; Morfu, 2003). Recent studies have also shown that noise can enhance image perception (Moss *et al.*, 2004; Simonotto *et al.*, 1997), autostereogram interpretation (Ditzinger *et al.*, 2000), human visual perception by microsaccades in the retina (Hongler *et al.*, 2003), and image processing (Vaudelle *et al.*, 1998; Chapeau-Blondeau, 2000; Histace and Rousseau, 2006; Blanchard *et al.*, 2007). The investigation of noise effects in nonlinear systems is undoubtedly of great interest in nonlinear signal processing or in image processing context (Zozar and Amblard, 1999, 2005).
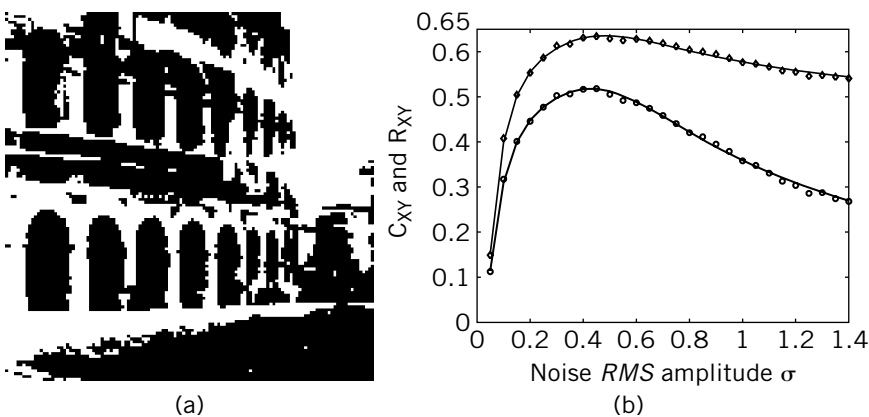

(a)

(b)

FIGURE 42   (a) Initial black-and-white image with $p1 = 0.437$. (b) Similarity measures from Eqs. (72) and (73) versus the noise RMS amplitude value σ for $V_{th} = 1.1$.

We thus propose to present the phenomenon of SR using the methodology exposed in proposed by Chapeau-Blondeau (2000). Moreover, to show a visual perception of the SR effect, we consider the black-and-white image of Figure 42a, where we note the probability p_1 to have a white pixel and $p_0 = 1 - p_1$ the probability to have a black one.

A gaussian white spatial noise $\eta_{i,j}$ with RMS amplitude value σ is added in each pixel $I_{i,j}$ of the initial image. The resulting noisy image is then threshold filtered with a threshold V_{th} to obtain the image I_b, according to the following threshold filtering rule:

$$\text{if } I_{i,j} + \eta_{i,j} > V_{th} \quad \text{then} \quad I_{b_{i,j}} = 1$$
$$\text{else} \quad I_{b_{i,j}} = 0. \tag{71}$$

The similarity between the two images I and I_b can then be quantified by the cross-covariance (Chapeau-Blondeau, 2000)

$$C_{II_b} = \frac{\left\langle \left(I - \langle I \rangle\right)\left(I_b - \langle I_b \rangle\right)\right\rangle}{\sqrt{\left\langle \left(I - \langle I \rangle\right)^2 \right\rangle \left\langle \left(I_b - \langle I_b \rangle\right)^2 \right\rangle}}, \tag{72}$$

or by

$$R_{II_b} = \frac{\left\langle II_b \right\rangle}{\sqrt{\left\langle I^2 \right\rangle \left\langle I_b^2 \right\rangle}}, \tag{73}$$

where $< . >$ corresponds to an average over the images.
These two similarity measures are defined by

$$R_{II_b} = \frac{p_1(1 - F_\eta(V_{th} - 1))}{\sqrt{p_1 \left[p_1 \left(1 - F_\eta(V_{th} - 1)\right) + \left(1 - p_1\right)\left(1 - F_\eta(V_{th})\right)\right]}}.$$

and

$$C_{II_b} = \frac{p_1(1 - F_\eta(V_{th} - 1)) - p_1 q_1}{\sqrt{(p_1 - p_1^2)(q_1 - q_1^2)}}.$$

AQ14

with $q_1 = p_1(1 - F_\eta(V_{th} - 1)) + (1 - p_1)(1 - F_\eta(V_{th}))$ and where F_η is the cumulative distribution function of the noise.

In the case of a gaussian white noise of RMS amplitude σ, the cumulative distribution function can be expressed as

$$F_\eta(u) = \frac{1}{2} + \frac{1}{2} er f \left(\frac{u}{\sqrt{2}\sigma} \right). \tag{74}$$

In Eq. (74) the error function is defined by $er f(u) = \frac{2}{\sqrt{\pi}} \int_0^u \exp(-t^2) dt$.

The two quantities expressed in Eqs. (72) and (73) are plotted versus the RMS noise amplitude σ in Figure 42b, where a resonant-like behavior reveals the standard stochastic resonance signature. Indeed, there exists an optimum amount of noise that maximizes the similarity measures in Eqs. (72) and (73). According to Figure 42b, this optimal noise RMS value is $\sigma = 0.4$.

To validate the similarity measures, we qualitatively analyze the pictures obtained for different noise amplitudes. It is confirmed in Figure 43 that the noise optimal value $\sigma = 0.4$ allows the best visual perception of the Coliseum through the nonlinear systems.

Even if the model of human visual perception is more complex than a standard threshold filtering (Bálya *et al.*, 2002), this simple representation is convenient to determine analytically the optimum amount of noise that provides the best visual perception of images via SR. Moreover, the SR phenomenon is shared by a wide class of nonlinear systems, including neural networks that also intervene in the process of image perception. Since neurons are basically threshold devices that are supposed to work in a noisy environment, the interest of considering noise effect seems to be of crucial importance in developing artificial intelligence applications that perfectly mimic the real behavior of nature. Therefore, for the next few decades we trust that one of the most interesting challenges could be completing the description of nonlinear models by including the contribution of noise effects.

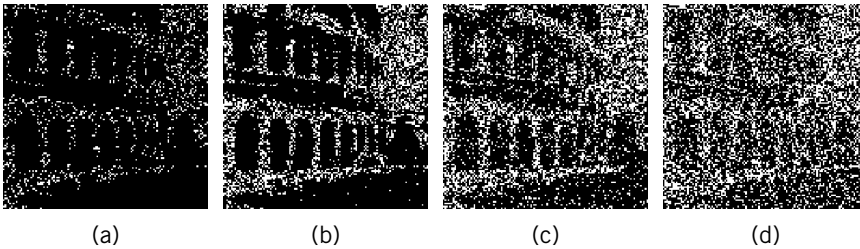(a)   (b)   (c)   (d)

FIGURE 43 (a), (b), (c), (d), Threshold filtered image with the rules (71) and a threshold $V_{th} = 1.1$ and with white gaussian noise with respective RMS noise amplitude $\sigma = 0.1$, $\sigma = 0.4$, $\sigma = 0.8$, $\sigma = 1.4$.

ACKNOWLEDGMENTS

APPENDIX A

Response of a Cell of an Overdamped Network

In the uncoupled case, and for $\alpha = 1/2$, a particle of displacement W follows

$$\frac{dW}{dt} = -W(W - \frac{1}{2})(W - 1). \tag{A1}$$

Separating the variables in Eq. (A1) yields

$$\frac{2dW}{W} - \frac{4dW}{W - 1/2} + \frac{2dW}{W - 1} = -dt, \tag{A2}$$

which can be integrated to obtain

$$\frac{W(W - 1)}{(W - 1/2)^2} = K \exp^{-\frac{1}{2}t}, \tag{A3}$$

where K is an integration constant. Equation (A3) can be arranged as a second-order equation in W

$$W^2\left(1 - Ke^{-\frac{1}{2}t}\right) - W\left(1 - Ke^{-\frac{1}{2}t}\right) - \frac{1}{4}Ke^{-\frac{1}{2}t} = 0. \tag{A4}$$

Provided that the discriminant is positive, the solutions are given by

$$W(t) = \frac{1}{2} \pm \frac{1}{2}\sqrt{\frac{1}{1 - Ke^{-\frac{1}{2}t}}}. \tag{A5}$$

Assuming that initially the position of the particle is $W(t = 0) = W^0$, the integration constant K can be expressed in the form

$$K = \frac{W^0(W^0 - 1)}{(W^0 - \frac{1}{2})^2}. \tag{A6}$$

Inserting the constant Eq. (A6) in the solution in Eq. (A5) leads to the following expression of the displacement:

$$W(t) = \frac{1}{2}\left(1 \pm \frac{|W^0 - \frac{1}{2}|}{\sqrt{(W^0 - \frac{1}{2})^2 - W^0(W^0 - 1)e^{-\frac{1}{2}t}}}\right). \tag{A7}$$

Assuming that when $t \mapsto +\infty$, the particle evolves to the steady states $W = 0$ for $W^0 < 1/2$ and $W = 1$ for $W^0 > 1/2$, we finally obtain the displacement of the particle with initial position W^0 as

$$W(t) = \frac{1}{2}\left(1 + \frac{W^0 - \frac{1}{2}}{\sqrt{(W^0 - \frac{1}{2})^2 - W^0(W^0 - 1)e^{-\frac{1}{2}t}}}\right). \qquad \text{(A8)}$$

APPENDIX B

Recall of Jacobian Elliptic Function

We recall here the properties of Jacobian elliptic functions used in Section II.B. These three basic functions—$cn(u, k)$, $sn(u, k)$, and $dn(u, k)$—play an important role in nonlinear evolution equations and arise from the inversion of the elliptic integral of first kind (Abramowitz and Stegun, 1970):

$$u(\psi, k) = \int_0^\psi \frac{dz}{\sqrt{1 - k\sin^2 z}}, \qquad \text{(B1)}$$

where $k \in [0; 1]$ is the elliptic modulus. The Jacobian elliptic functions are defined by

$$sn(u, k) = \sin(\psi), cn(u, k) = \cos(\psi), dn(u, k) = \sqrt{1 - k\sin^2(\psi)}. \quad \text{(B2)}$$

This definition involves the following properties for the derivatives:

$$\frac{d\, sn(u, k)}{du} = cn(u, k)dn(u, k),$$

$$\frac{d\, cn(u, k)}{du} = -sn(u, k)dn(u, k),$$

$$\frac{d\, dn(u, k)}{du} = -ksn(u, k)cn(u, k). \qquad \text{(B3)}$$

Considering the circular function properties, we also have

$$sn^2(u, k) + cn^2(u, k) = 1. \qquad \text{(B4)}$$

Moreover, using the result in Eq. (B2), we obtain the following identity:

$$dn^2(u,k) + ksn^2(u,k) = 1. \tag{B5}$$

APPENDIX C

Evolution of an Overdamped Particle Experiencing a Multistable Potential

The equation of motion of an overdamped particle submitted to the sinusoidal force in Eq. (56) can be expressed as

$$\frac{dW}{dt} = -\beta(n-1)\sin\left[2\pi(n-1)W\right], \tag{C1}$$

where W represents the particle displacement.

The steady states of the system are deduced from the zeros of the non-linear force. Using the methodology exposed in Section II.A.1, we can establish that the roots of the nonlinear force correspond alternatively to unstable and stable steady states. If k is an integer, the unstable and stable states of the system are written, respectively, as follows:

$$W_{thk} = \frac{k}{(n-1)} \qquad W_k^* = \frac{2k+1}{2(n-1)} \qquad k \in \mathbb{Z}. \tag{C2}$$

Separating the variables of Eq. (C1), we obtain

$$\frac{dW}{\sin\left[2\pi(n-1)W\right]} = -\beta(n-1)dt. \tag{C3}$$

Using the identity $\sin(2a) = 2\sin a \cos a$, Eq. (C3) becomes

$$\frac{dW}{\tan\left[\pi(n-1)W\right]\cos^2\left[\pi(n-1)W\right]} = -\beta(n-1)dt. \tag{C4}$$

Next, considering the derivative of the tangent function in Eq. (C4), yields

$$\frac{1}{\pi(n-1)}\int_0^t \frac{d\tan\left[\pi(n-1)W\right]}{\tan\left[\pi(n-1)W\right]} = -\int_0^t 2\beta(n-1)dt. \tag{C5}$$

A direct integration of Eq. (C5) gives

$$\tan\left[\pi(n-1)W\right] = \tan\left[\pi(n-1)W^0\right]e^{-\beta(n-1)^2 2\pi t}, \qquad \text{(C6)}$$

where W^0 denotes the initial position of the particle.

Inverting the tangent function provides straightforwardly the solution of Eq. (C1) in the form

$$W(t) = \frac{1}{\pi(n-1)}\left[\arctan\left(\tan\left(\pi(n-1)W^0\right)e^{-\beta(n-1)^2 2\pi t}\right)\right] + \frac{k}{n-1},$$
$$\text{(C7)}$$

where k is an integer coming from the tangent inversion.

Note that from a physical point of view, k must ensure that the particle position evolves toward one of the stable states of the system for a sufficiently long time, that is, when $t \mapsto +\infty$.

Indeed, for an initial condition between two consecutive unstable steady states, the asymptotic behavior of the uncoupled network can reduce to the following rule:

$$if \; \frac{2k-1}{2(n-1)} < W^0 < \frac{2k+1}{2(n-1)} \qquad W(t \mapsto +\infty) = \frac{k}{(n-1)} \qquad \text{(C8)}$$

This rule can be transformed to yield

$$if \; k - \frac{1}{2} < (n-1)W^0 < k + \frac{1}{2} \qquad W(t \mapsto +\infty) = \frac{k}{(n-1)} \qquad \text{(C9)}$$

Finally, identifying Eq. (C7) with Eq. (C9) when $t \mapsto +\infty$, we deduce that k must be the nearest integer of $W^0(n-1)$.

APPENDIX D

Perona and Malik Anisotropic Diffusion Algorithm

We recall here the algorithm introduced by Perona and Malik to compute their method based on anisotropic diffusion equation. The anisotropic diffusion Eq. (69) can be discretized with the time step dt

to obtain

$$I_s^{t+1} = I_s^t + \frac{dt}{\eta_s} \sum_{p \in Nr} g(\nabla I_{s,p}) \nabla I_{s,p}. \tag{D1}$$

In Eq. (D1), I_s^t represents the brightness of the pixel located at the position s in a discrete 2D grid that corresponds to the filtered image after a processing time t. η_s is the number of neighbors of the pixel s, that is, 4, except for the image edge, where $\eta_s = 3$ and for the image corners where $\eta_s = 2$. The spatial neighborhood of the pixel s is noted Nr. The local gradient $\nabla I_{s,p}$ can be estimated by the difference of brightness between the considered pixel s and its neighbor p:

$$\nabla I_{s,p} = I_p - I_s^t, \quad p \in Nr. \tag{D2}$$

Finally, the description of the system is completed by defining the edge stopping function $g(x)$ as the Lorentzian function:

$$g(x) = \frac{1}{1 + \frac{x^2}{K^2}}, \tag{D3}$$

where K is a positive parameter.

REFERENCES

Abramowitz, M., and Stegun, I. A. (1970). *Handbook of Mathematical Functions*. Dover, New York, p. 569.

Acosta-Serafini, P., Ichiro, M., and Sodini, C. (2004). A linear wide dynamic range CMOS image sensor implementing a predictive multiple sampling algorithm with overlapping integration intervals. *IEEE J. Solid-State Circuits* **39**, 1487–1496.

Adamatzky, A., and de Lacy Costello, B. (2003). On some limitations of reaction-diffusion chemical computers in relation to Voronoi diagram and its inversion, *Phys. Lett. A* **309**, 397–406.

Adamatzky, A., de Lacy Costello, B., Melhuish, C., and Ratcliffe, N. (2004). Experimental implementation of mobile robot taxis with onboard Belousov-Zhabotinsky chemical medium. *Mater. Sci. Eng. C* **24**, 541–548.

Adamatzky, A., de Lacy Costello, B., and Ratcliffe, N. (2002). Experimental reaction-diffusion preprocessor for shape recognition. *Phys. Lett. A* **297**, 344–352.

Agladze, K., Magone, N., Aliev, R., Yamaguchi, T., and Yoshikawa, K. (1977). Finding the optimal path with the aid of chemical wave. *Physica D* **106**, 247–254.

Agrawal, G. P. (2002). *Fiber-Optic Communication Systems*, 3rd ed., Wiley Inter-Science, New York.

Arena, P., Basile, A., Bucolo, M., and Fortuna, L. (2003). An object oriented segmentation on analog CNN chip. *IEEE Trans. Circ. Syst. I* **50**, 837–846.

AQ

Bálya, D., Roska, B., Roska, T., and Werblin, F. S. (2002). A CNN framework for modeling parallel processing in a mammalian retina. *Int. J. Circ. Theor. Appl.* **30**, 363–393.

Blanchard, S., Rousseau, D., Gindre, D., and Chapeau-Blondeau, F. (2007). Constructive action of the speckle noise in a coherent imaging system. *Optics Lett.* **32**, 1983–1985.

Barbay, S., Giacomelli, G., and Marin, F. (2001). Noise-assisted transmission of binary information: theory and experiment. *Phys. Rev. E* **63**, 051110/1–9.

Báscones, R., Garcìa-Ojalvo, J., and Sancho, J. M. (2002). Pulse propagation sustained by noise in arrays of bistable electronic circuits. *Phys. Rev. E* **65**, 061108/1–5.

Beeler, G. W., and Reuter, H. (1997). Reconstruction of the action potentials of ventricular myocardial fibers. *J. Physiol.* **268**, 177–210.

Benzi, R., Parisi, G., Sutera, A., and Vulpiani, A. (1982). Stochastic resonance in climatic change. *Tellus* **34**, 10–16.

Binczak, S., Comte, J. C., Michaux, B., Marquié, P., and Bilbault, J. M. Experiments on a nonlinear electrical reaction-diffusion line. *Electron. Lett.* **34**, 1061–1062.

Black, M. J., Sapiro, G., Marimont, D. H., and Heeger, D. (1998). Robust anisotropic diffusion *IEEE Trans. On Image Processing* **7**, 421–432.

Bressloff, P. C., and Rowlands, G. (1997). Exact travelling wave solutions of an "integrable" discrete reaction-diffusion equation. *Physica D* **106**, 255–269.

Caponetto, R., Fortuna, L., Occhipinti, L., and Xibilia, M. G. (2003). Sc-CNNs for chaotic signal applications in secure communication systems, *Int. J. Bifurcat. Chaos*, **13**, 461–468.

Carmona Galan, R., Jimenez-Garrido, F., Dominguez-Castro, R., Espejo, S., Roska, T., Rekeczky, C., Petras, I., and Rodriguez-Vazquez, A. (2003). A bio-inspired two-layer mixed-xignal flexible programmable chip for early vision. *IEEE Trans. Neural Networ.* **14**, 13131–336.

Chapeau-Blondeau, F. (1999). Noise-assisted propagation over a nonlinear line of threshold elements *Electr. Lett.* **35**, 1055–1056.

Chapeau-Blondeau, F. (2000). Stochastic resonance and the benefit of noise in nonlinear systems. *Lect Notes Phys.* **550**, 137–155.

Chen, H-C., Hung, Y-C., Chen, C-K., Liao, T-L., and Chen, C-K. (2006). Image processing algorithms realized by discrete-time cellular neural networks and their circuit implementation. *Chaos Soliton Fract.* **29**, 1100–1108.

Chua, L. O., and Yang, L. (1998a). Cellular neural networks: Theory, *IEE Trans. Circ. Syst.* **35**, 1257–1272.

Chua, L. O., and Yang, L. (1988b). Cellular neural networks: Applications. *IEE Trans. Circ. Syst.* **35**, 1273–1290.

Chua, L. O. (1998). CNN: A paradigm for complexity (World Scientific Series on Nonlinear Science, Series A, vol. 31). World Scientific Publishing, Singapore.

Comte, J. C. (1996). Etude d'une ligne non linéaire de type Nagumo-Neumann. *DEA Laboratory report LIESIB, Dijon, France*.

Comte, J. C., and Marquié, P. (2002). Generation of nonlinear current-voltage characteristics. A general method. *Int. J. Bifurc. Chaos* **12**, 447–449.

Comte, J. C., Marquié, P., and Bilbault, J. M. (2001). Contour detection based on nonlinear discrete diffusion in a cellular nonlinear network. *Int. J. Bifurc. Chaos* **11**, 179–183.

Comte, J. C., Marquié, P., Bilbault, J. M., and Binczak, S. (1998). Noise removal using a two-dimensional diffusion network *Ann. Telecom.* **53**, 483–487.

Comte, J. C., Marquié, P., and Remoissenet, M. (1999). Dissipative lattice model with exact travelling discrete kink-soliton solutions: Discrete breather generation and reaction diffusion regime. *Phys. Rev. E* **60**, 7484–7489.

Comte, J. C., and Morfu, S. (2003). Stochastic resonance: Another way to retrieve subthreshold digital data. *Phys. Lett. A* **309**, 39–43.

Comte, J. C., Morfu, S., and Marquié, P. (2001). Propagation failure in discrete bistable reaction-diffusion systems: Theory and experiments. *Phys. Rev. E* **64**, 027102/1–4.

Cuomo, K. M., and Oppenheim, A. V. (1993). Circuit implementation of synchronized chaos with applications to communications. *Phys. Rev. Lett.* **71**, 65–68.

Czuni, L., and Sziranyi, T. (2001). Motion segmentation and tracking with edge relaxation and optimization using fully parallel methods in the cellular nonlinear network architecture. *Real-Time Imaging* **7**, 77–95.

Dedieu, H., Kennedy, M. P., and Hasler, M. (1993). Chaos shift keying: Modulation and demodulation of a chaotic carrier using self-synchronizing Chua's circuits. *IEEE Trans. Circ. Syst. Part II* **40**, 634–642.

Ditzinger, T., Stadler, M., Strüber, D., and Kelso, J. A. S. (2000). Noise improves three-dimensional perception: Stochastic resonance and other impacts of noise to the perception of autostereograms, *Phys Rev E* **62**, 2566–2575.

Duan, F., and Abbott, D. (2005). Signal detection for frequency-shift keying via short-time stochastic resonance. *Phys. Lett. A* **344**, 401–410.

Dudek, P. (2006). Adaptive sensing and image processing with a general-purpose pixel-parallel sensor/processor array integrated circuit. *International Workshop on Computer Architecture for Machine Perception and Sensing*, Montreal, 2006, 1–6.

El-Gamal, A., Yang, D., and Fowler, B. (1999). Pixel level processing—Why, what and how? *Proc. SPIE Electr. Imaging '99 Conference* **3650**, 2–13.

Erneux, T., and Nicolis, G. (1993). Propagating waves in discrete bistable reaction-diffusion systems. *Physica D* **67**, 237–244.

Espejo, S., Rodriguez-Vázquez, A., Carmona, R., and Dominguez-Castro, R. (1996). A 0.8-µm CMOS programmable analog-array-processing vision-chip with local logic and image-memory. *European Solid-State Devices and Reliability Conference*, Neuchatel, 1996, pp. 276–279.

Espejo, S., Dominguez-Castro, R., Linan, G., and Rodriguez-Vázquez, A. (1998). A 64 × 64 CNN universal chip with analog and digital I/O. *Proc. 5th IEEE Int. Conf. Electronics, Circuits and Systems*, 1998, pp. 203–206.

Fife, P. C. (1970). *Mathematical Aspects of Reacting and Diffusing Systems* (Lecture Notes in Biomathematics, vol. 28). Springer-Verlag, New York.

Fisher, R. A. (1937). The wave of advance of advantageous genes. *Ann. Eugen.* **7**, 355–369.

Fossum, E. (1993). Active pixel sensors: Are CCDs dinosaurs? *Int. Soc. Opt. Eng. (SPIE)* **1900**, 2–14.

Fossum, E. (1997). CMOS image sensor: Electronic camera on a chip. *IEEE Trans. Electr. Dev.* **44**, 1689–1698.

Gammaitoni, L., Hänggi, P., Jung, P., and Marchesoniand, F. (1998). Stochastic resonance. *Rev. Mod. Phys.* **70**, 223–282.

Gonzalez, R. C., and Wintz, P. (1997). *Digital Image Processing*, 2nd ed. Addison-Wesley.

Henry, D. (1981). *Geometric Theory of Semilinear Parabolic Equations*. Springer-Verlag, New York.

Hirota, R., and Suzuki, K. (1970). Studies on lattice solitons by using electrical networks. *J. Phys. Soc. Jpn.* **28**, 1366–1367.

Histace, A., and Rousseau, D. (2006). Constructive action of noise for impulsive noise removal in scalar images. *Electr. Lett.* **42**, 393–395.

Holden, A. V., Tucker, J. V., and Thompson, B. C. (1991). Can excitable media be considered as computational systems? *Physica D* **49**, 240–246.

Hongler, M., De Meneses, Y., Beyeler, A., and Jacquot, J. (2003). The resonant retina: Exploiting vibrational noise to optimally detect edges in an image. *IEEE Trans. Patt. Anal. Machine Intell.* **25**, 1051–1062.

Izhikevitch, E. M. (2007). *Dynamical Systems in Neuroscience: The Geometry of Excitability and Bursting.* MIT Press, Cambridge, Massachussetts.

Jäger, D. (1985). Characteristics of travelling waves along the nonlinear transmission line for monolithic integrated circuits: a review, *Int. J. Electron.* **58**, 649–669.

Julián, P., and Dogaru R. (2002). A piecewise-linear simplicial coupling cell for CNN gray-level image processing. *IEEE Trans. Circ. Syst. I* **49**, 904–913.

Keener, J. P. (1987). Propagation and its failure in coupled systems of discrete excitable cells. *SIAM J. Appl. Math.* **47**, 556–572.

Keener, J. P. (2000). Homogeneization and propagation in the bistable equation. *Physica D* **136**, 1–17.

Kladko, K. (2000). Universal scaling of wave propagation failure in arrays of coupled nonlinear cells. *Phys. Rev. Lett.* **84**, 4505–4508.

Kozlowski, L., Rossi, G., Blanquart, L., Marchesini, R., Huang, Y., Chow, G., Richardson, J., and Standley, D. (2005). Pixel noise suppression via SoC management of target reset in a 1920 × 1080 CMOS image sensor. *IEEE J. Solid-State Circ.* **40**, 2766–2776.

Kuhnert, L. (1986). A new optical photochemical device in a light-sensitive chemical active medium. *Nature* **319**, 393–394.

Kuhnert, L., Agladze K. I., and Krinsky, V. I. (1989). Image processing using light-sensitive chemical waves. *Nature* **337**, 244–247.

Kuusela, T. (1995). Soliton experiments in transmission lines. *Chao Solitons Fract.* **5**, 2419–2462.

Kwok, H. S., and Tang, W. K. S. (2007). A fast image encryption system based on chaotic maps with finite precision representation. *Chaos Solitons Fract.* **47**, 1518–1529.

Lindner, J. F., Chandramouli, S., Bulsara Adi, R., Löcher, M., and Ditto, W. L. (1998). Noise enhanced propagation. *Phys. Rev. Lett.* **81**, 5048–5051.

Litwiller, D. (2001). CCD vs. CMOS: Facts and fiction. *Photon. Spectra* ·(Special Issue)·, 154–158.

Loinaz, M., Singh, K., Blanksby, A., Inglis, D., Azadet, K., and Ackland, B. (1998). A 200-mv 3.3-v CMOS color camera IC producing 352 × 288 24-b Video at 30 frames/s. *IEEE J. Solid-State Circ.* **33**, 2092–2103.

Longtin, A. (1993). Stochastic resonance in neuron models. *J. Stat. Phys.* **70**, 309–327.

Marquié, P., Bilbault, J. M., and Remoissenet, M. (1995). Observation of nonlinear localized modes in an electrical lattice. *Phys. Rev. E* **51**, 6127–6133.

Marquié, P., Binczak, S., Comte, J. C., Michaux, B., and Bilbault, J. M. (1998). Diffusion effects in a nonlinear electrical lattice. *Phys. Rev. E* **57**, 6075–6078.

Morfu, S. (2002c). *Etude des défauts et perturbations dans les réseaux électroniques dissipatifs non linéaires: Applications à la transmission et au traitement du signal*. Ph. D. thesis, Laboratory LE2I, Dijon, France.

Morfu, S. (2003). Propagation failure reduction in a Nagumo chain. *Phys. Lett. A* **317**, 73–79.

Morfu, S. (2005). Image processing with a cellular nonlinear network. *Phys. Lett. A* **343**, 281–292.

Morfu, S., and Comte, J. C. A. (2004). Nonlinear oscillators network devoted to image processing. *Int. J. Bifurc. Chaos* **14**, 1385–1394.

Morfu, S., Bossu, J., and Marquié, P. Experiments on an electrical nonlinear oscillators network. *Int. J. Bifurcat. Chaos*, **17**, 3535–3538 (2007). To appear.

Morfu, S., Bossu, J., Marquié, P., and Bilbault, J. M. (2006). Contrast enhancement with a nonlinear oscillators network. *Nonlinear Dynamics* **44**, 173–180.

Morfu, S., Comte, J. C., and Bilbault, J. M. (2003). Digital information receiver based on stochastic resonance. *Int. J. Bifurc. Chaos* **13**, 233–236.

Morfu, S., Comte, J. C., Marquié, P., and Bilbault, J. M. (2002). Propagation failure induced by coupling inhomogeneities in a nonlinear diffusive medium. *Phys. Lett. A* **294**, 304–307.

Morfu, S., Nekorkin, V. B., Bilbault, J. M., and Marquié, M. (2002). The wave front propagation failure in an inhomogeneous discrete Nagumo chain: Theory and experiments. *Phys. Rev. E* **66**, 046127/1–8.

Morfu, S., Nofiélé, B., and Marquié, P. (2007). On the use of multistability for image processing. *Phys. Lett. A* **367**, 192–198.

Moss, F., Ward, L. M., and Sannita, W. G. (2004). Stochastic resonance and sensory information processing: A tutorial and review of application. *Clin. Neurophysiol.* **115**, 267–281.

Murray, J. D. (1989). *Mathematical Biology*. Springer-Verlag, Berlin.

Nagumo, J., Arimoto, S., and Yoshisawa, S. (1962). An active pulse transmission line simulating nerve axon. *Proc. IRE* **50**, 2061–2070.

Nagashima, H., and Amagishi, Y. (1978). Experiments on the Toda lattice using nonlinear transmission line. *J. Phys. Soc. Jpn.* **45**, 680–688.

Nozaki, D., Mar, D. J., Grigg, P., and Collins, J. J. (1999). Effects of colored noise on stochastic resonance in sensory neurons. *Phys. Rev. Lett.* **82**, 2402–2405.

Occhipinti, L., Spoto, G., Branciforte, M., and Doddo, F. (2001). Defects detection and characterization by using cellular neural networks. *IEEE Int. Symposium on Circuits and Systems ISCAS* 3, Sydney, Australia, May 6–9, 2001, pp. 481–484.

Paquerot, J. F., and Remoissenet, M. (1994). Dynamics of nonlinear blood pressure waves in large arteries. *Phys. Lett. A* **194**, 77–82.

Perona, P., and Malik, J. (1990). Scale-space and edge detection using anisotropic diffusion. *IEEE Trans. Patt. Anal. Machine Intell.* **12**, 629–639.

Petras, I., Rekeczky, C., Roska, T., Carmona, R., Jimenez-Garrido, F., and Rodriguez-Vazquez, A. (2003). Exploration of spatial-temporal dynamic phenomena in a 32×32-cells stored program 2-layer CNN universal machine chip prototype. *J. Circ. Syst. Computers* **12**, 691–710.

Rambidi, N. G., Shamayaev, K. E., and Peshkov, G. Y. (2002). Image processing using light-sensitive chemical waves. *Phys. Lett. A*, **298**, 2002, 375–382.

Rambidi, N. G., and Yakovenchuk, D. (2001). Chemical reaction-diffusion implementation of finding the shortest paths in a labyrinth. *Phys. Rev. E* **63**, 026607/1–6.

Rekeczky, C., Tahy, A., Vegh, Z., and Roska, T. (1999). CNN-based spatio-temporal nonlinear in filtering and endocardial boundary detection in echocardiography. *Int. J. Circuit Theory Applicat.* **27**, 171–207.

Remoissenet, M. (1999). *Waves Called Solitons: Concepts and Experiments*, 3rd rev. enlarged ed., Springer-Verlag, Berlin, p. 284.

Roska, T., and Rodriguez-Vazquez, A. (2000). Review of CMOS implementations of the CNN universal machine-type visual microprocessors. *ISCAS 2000 IEEE International Symposium on Circuits and Systems*, Geneva, 2000, pp. 120–123.

Sakakibara, M., Kawahito, S., Handoko, D., Nakamura, N., Higashi, M., Mabuchi, K., and Sumi, H. (2005). A high-sensitivity CMOS image sensor with gain-adaptative column amplifiers/*IEEE J. Solid-State Circ.* **40**, 1147–1156.

Scott, A. C. (1970). *Active and Nonlinear Wave Propagation in Electronics*. Wiley Interscience, New York.

Scott, A. (1999). *Nonlinear Science: Emergence and Dynamics of Coherent Structures* (Oxford Applied and Engineering Mathematics, 8), Oxford University Press, New York.

Seitz, P. (2000). Solid-state image sensing. *Handbook of Computer Vision and Applications* **1**, 165–222.

Serra, J. (1986). Introduction to mathematical morphology. *Comput. Vision Graph*. **35**, 283–305.

Short, K. M., and Parker, A. T. (1998). Unmasking a hyperchaotic communication scheme. *Phys. Rev. E* **58**, 1159–1162.

Simonotto, E., Riani, M., Seife, C., Roberts, M., Twitty, J., and Moss, F. (1997). Visual perception of stochastic resonance. *Phys. Rev. Lett.* **78**, 1186–1189.

Smith, S., Hurwitz, J., Torrie, M., Baxter, D., Holmes, A., Panaghiston, M., Henderson, R., Murrayn, A., Anderson, S., and Denyer, P. A single-chip 306×244-pixel CMOS NTSC video camera. *In* "Solid-State Circuits Conference, 1998. Digest of Technical Papers. 45th ISSCC 1998 IEEE International," pp. 170–171. 432, San Francisco.

Stocks, N. G., and Manella, R. (2001). Generic noise-enhanced coding in neuronal arrays. *Phys. Rev. E* **64**, 030902/1–4.

Taniuti, T., and Wei, C. C. (1968). Reductive perturbation method in nonlinear wave propagation. *J. Phys. Soc. Jap.* **21**, 941–946.

Taniuti, T., and Yajima, N. (1969). Perturbation method for a nonlinear wave modulation. *J. Math. Phys.* **10**, 1369–1372.

Tetzlaff. R. (ed). (2002). *Cellular Neural Networks and Their Applications*, World Scientific Publishing, Singapore.

Teuscher, C., and Adamatzky, A (eds). (2005). *Proceedings of the 2005 Workshop on Unconventional Computing, From Cellular Automata to Wetware*. Luniver Press, Lightning Source.

Toda, M. (1967). Wave propagation in anharmonic lattices. *J. Phys. Soc. Jpn.* **23**, 501–506.

Udaltsov, V. S., Goedgebuer, J. P., Larger, L., Cuenot, J. B., Levy, P., and Rhodes, W. T. (2003). Cracking chaos-based encryption systems ruled by nonlinear time delay differential equations. *Phys. Lett. A* **308**, 54–60.

Vaudelle, F., Gazengel, J., Rivoire, G., Godivier, X., and Chapeau-Blondeau, F. (1998). Stochastic resonance and noise-enhanced transmission of spatial signals in optics: The case of scattering. *J. Opt. Soc. Am. B* **13**, 2674–2680.

Venetianer, P. L., Werblin, F., Roska, T., Chua, L. O. (1995). Analogic CNN algorithms for some image compression and restoration tasks. *IEEE Trans. Circ. Syst. I* **42**, 278–284.

Yadid-Pecht, O., and Belenky, A. (2003). In-pixel autoexposure CMOS APS. *IEEE J. Solid-State Circ.* **38**, 1425–1428.

Yamgoué, S. B., Morfu, S., and Marquié, P. (2007). Noise effects on gap wave propagation in a nonlinear discrete LC transmission line. *Phys. Rev E* **75**, 036211/1–036211/1–7.

Yu, W., and Cao, J. (2006). Cryptography based on delayed chaotic neural networks. *Phys Lett. A* **356**, 333–338.

Zakharov, V. E., and Wabnitz, S. (1998). Optical solitons: Theoretical challenges and industrial perspectives. Springer-Verlag, Berlin.

Zozor, S., and Amblard, P. O. (1999). Stochastic resonance in discrete time nonlinear AR(1) models. *IEEE Trans. Signal Proc.* **49**, 109–120.

Zozor, S., and Amblard, P. O. (2003). Stochastic resonance in locally optimal detectors. *IEEE Trans. Signal Proc.* **51**, 3177–3181.

Zozor, S. and Amblard P. O. (2005). Noise aidded processing: revisiting dithering in a Sigma-Delta quantizer. *IEEE Trans. Signal Proc.* **53**, 3202–3210.

AQ Please check all text citations carefully; in some instances you listed only a first name (no *et al.* but it appears that the "*et al.*" would complete the citation correcty; Please see the "**et al.?**" notes on the edited manuscript.

AQ1 Changes OK?

AQ2 The term "purproted" ok or use "suggested"?

AQ3 The word "by" should be "for"?

AQ4 Should this be encryption? It is not exactly the same as cryptography (in English).

AQ5 Is this an equation no.?

AQ6 Add space before V's?

AQ7 Edits OK?

AQ8 Changes correct?

AQ9 What is transient?

AQ10 Should the Conclusion section follow Outlooks?

AQ11 Please provide the expansion for the CMOS, DRAMs and VLSI.

AQ12 Change OK or use smaller?

AQ13 Is it a & b?

AQ14 spell out?